ADVANCING
EARTH AND
SPACE SCIENCE

JGR Oceans

RESEARCH ARTICLE

10.1029/2022JC018752

Off-Coast Phytoplankton Bloom in the Taiwan Strait During the Northeasterly Monsoon Wind Relaxation Period

Zhonghua Zhao[1,2], Lie-Yauw Oey[3], Bangqin Huang[1,4,5], Wenfang Lu[6], and Yuwu Jiang[1,2,5]

[1]State Key Laboratory of Marine Environmental Science, Xiamen University, Xiamen, P. R. China, [2]College of Ocean and Earth Sciences, Xiamen University, Xiamen, P. R. China, [3]Princeton University, Princeton, NJ, USA, [4]Fujian Provincial Key Laboratory of Coastal Ecology and Environmental Studies, Xiamen University, Xiamen, P. R. China, [5]National Observation and Research Station for the Taiwan Strait Marine Ecosystem, Xiamen University, Xiamen, P. R. China, [6]School of Marine Sciences, Sun Yat-Sen University, and Southern Marine Science and Engineering Guangdong Laboratory (Zhuhai), Zhuhai, P. R. China

Key Points:

- Multi-source observations confirm the significant growth of phytoplankton during the northeasterly monsoon relaxation in the Taiwan Strait (TWS)
- High-resolution cruise and model results show vigorous submesoscale instabilities near the along-shore front during blooming
- Instability-induced restratification primarily favors off-coast phytoplankton growth within the upper 10-m of the mixed layer

Supporting Information:

Supporting Information may be found in the online version of this article.

Correspondence to:

Y. Jiang,
ywjiang@xmu.edu.cn

Citation:

Zhao, Z., Oey, L.-Y., Huang, B., Lu, W., & Jiang, Y. (2022). Off-coast phytoplankton bloom in the Taiwan Strait during the northeasterly monsoon wind relaxation period. *Journal of Geophysical Research: Oceans*, *127*, e2022JC018752. https://doi.org/10.1029/2022JC018752

Received 18 APR 2022
Accepted 9 SEP 2022

Abstract

This study applied cruise, model, and satellite data to analyze the off-coast phytoplankton blooming during the late fall to early spring monsoon period in the Taiwan Strait when northeasterly wind prevails. Based on the composite and self-organizing map analyses, the three data sets consistently show high chlorophyll-a concentration near the along-shore front during the down-front northeasterly wind relaxation period while lower concentration when relatively strong wind is persistent. Meanwhile, the off-coast blooming always coincides with intense near-surface stratification when the northeasterly wind relaxes. Diagnoses of balanced Richardson number, Ertel potential vorticity and instability energy budget from high-resolution cruise observations and model results demonstrate that vigorous submesoscale symmetric and baroclinic instabilities can develop near the along-shore front under the down-front NE wind. Diagnoses of modeled buoyancy and chlorophyll-a budget equations further suggest the submesoscale instabilities lead to rapid near-surface restratification and offshore stretching of the along-shore front within the upper 10-m of the mixed layer when the down-front NE wind relaxes, favoring the surface 10-m phytoplankton growth. As comparison, contribution of the larger-scale advection related with geostrophic adjustment and Ekman transport to the chlorophyll-a increment reached beyond the middle layer of ~20-m depth.

Plain Language Summary

Cruise and satellite observations presented three phytoplankton growth scenarios depending on dominant wind characteristics from winter to early spring in the Taiwan Strait. Off-coast blooms with significantly higher chlorophyll-a concentration were observed during the northeasterly monsoon relaxation period compared with persistent northeasterly wind or southwesterly wind periods. High-resolution cruise and model results indicate that submesoscale instability-induced near-surface restratification near the coastal front along mainland China's coast triggers the off-coast bloom. This study has practical significances on harmful algal bloom prediction and fishery development near coastal waters.

1. Introduction

The Taiwan Strait (TWS; Figure 1) is an important waterway that connects the East China Sea (ECS) and South China Sea (SCS). It has complex topography and hydrodynamics. The currents and marine ecosystem of the TWS are affected by the East Asia Monsoon. Strong northeasterly (NE) monsoon prevails over the strait from September to April, and southwesterly (SW) monsoon prevails from May to August (Chen et al., 2006; Hong, Chai, et al., 2011). Under the NE monsoon, the China Coastal Current (CCC, Figures 1a and S7 in Supporting Information S1) (Oey et al., 2014) brings fresh, cold, low-density, and nutrient-rich water south along the western coast of the TWS. Wu et al. (2013) reported that the CCC is driven by both the NE wind and buoyancy; Meanwhile, the Southern Mixing Current (SMC, Figures 1a and S7 in Supporting Information S1) (Wang et al., 2016) carries saline, warm, high-density, and nutrient-poor mixed water from the Kuroshio and South China Seas into the strait along the Penghu Channel (Hong, Chai, et al., 2011; Hu et al., 2010). The SMC is mainly driven by the ever-existing northward pressure gradient force all year round (Yang, 2007). As a result, an intense, off-coast front separating the two water masses of different densities is often formed in the northern strait at about 50–60 km offshore from the mainland coast (Hu, 2002). Due to complex coastal bathymetry and the influence of highly variable NE monsoon winds, the front displays considerable spatiotemporal variability (Hu, 2002; Liao et al., 2013; Lin et al., 2016; Oey et al., 2014; Wang et al., 2016). Although the NE wind generally prevails from late fall to early spring, it frequently relaxes and sometimes

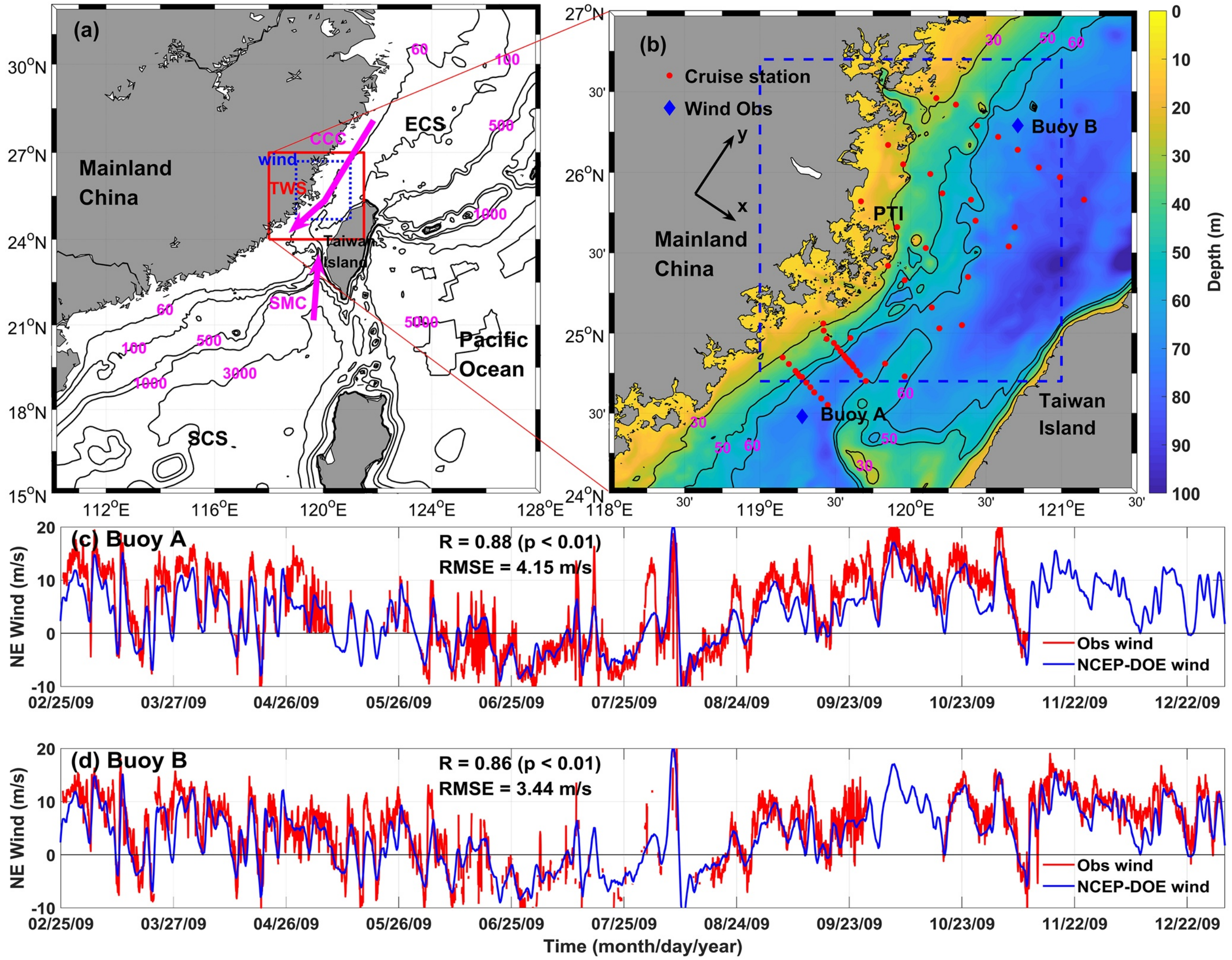

Figure 1. Location of the Taiwan Strait (TWS) (a) with bottom topography (contours, units: m) and cruise stations (red dots) in the northern strait (b). (a) TWS, East China Sea (ECS), and South China Sea (SCS) denote the Taiwan Strait, East China Sea, and South China Sea, respectively. China Coastal Current (CCC) and Southern Mixing Current (SMC) denote the China Coastal Current and Southern Mixing Current. The red box indicates the location of the inset (b). The blue dashed box in (a and b) indicates the spatial domain of the NCEP wind data used in computing the NE wind timeseries from 1998 to 2018. (b) Color shading shows the bottom topography. The black solid lines show 30, 50, and 60-m isobath. The blue diamonds indicate the location of the wind observation Buoys A and B The positive cross-shore and along-shore directions are indicated by the arrows of *x* and *y*, respectively. PTI denotes the Pingtan Island. Time series of the daily running-mean NCEP NE wind (blue line) and the observed NE wind (red line) measured by Buoys A (c) and B (d) in the TWS from February 25 to 31 December 2009.

turns southwesterly for short synoptic periods (Hu et al., 2010; Zhao et al., 2020). With the relaxation of the NE wind, the SMC is allowed to flow northward into the TWS (Hu et al., 2010). Generally, the NE wind can intensify the along-shore front by inducing Ekman transport of denser fluid over lighter, which is referred to as a down-front wind (Mahadevan et al., 2012; Thomas & Lee, 2005). While the SW wind acts as an up-front wind, which intensifies stratification near the surface Ekman layer depth (Chang & Oey, 2011; Mahadevan et al., 2012).

The nutrient-rich CCC contributes to the growth of phytoplankton and increases primary production in the TWS. Based on data collected in the winter and early spring of the period of 1983–1984, Zhang (2001) reported an average chlorophyll-a concentration (Chl-a) of 0.88 mg·m^{-3} and average nitrate and phosphate concentrations of 9.55 μmolN·L^{-1} and 0.63 μmolP·L^{-1}, respectively. The corresponding N/P ratio (15.2:1) was close to the Redfield ratio (16:1), which may be the result of nutrient accumulation (Ji & Huang, 1992). Therefore, in winter and early spring, phosphorus or nitrogen limitation cannot inhibit primary production (Smith, 1984). The nitrate pattern approximately correlates with that of the nutrients in the TWS.

However, despite the high-nutrient standing stock, phytoplankton biomass in the northern strait is relatively low during boreal winter and early spring (Zhang, 2001), although episodes of anomalously high Chl-a can occur in winter (Wang et al., 2016; Zhang & Huang, 2000). There are two primary reasons for the relatively low Chl-a in the TWS, namely, low water temperature (Zhang & Huang, 2000) and intensive turbulent mixing due to strong NE monsoon winds (Huang & Oey, 2015; Huisman et al., 1999, 2004, Taylor & Ferrari, 2011a). The critical depth theory suggests that a bloom begins when the mixed-layer becomes shallower than a critical depth (Sverdrup, 1953), whereas the critical turbulence theory suggests that a bloom develops when turbulent mixing is less than a critical turbulence level (Huisman et al., 1999, 2004).

Wang et al. (2016) suggested that the relaxation of the NE wind can trigger off-coast phytoplankton blooms based on a coupled physical-biological model. Phytoplankton blooms are also frequently observed in frontal zones. Previous studies have demonstrated that water column stability can influence phytoplankton growth. Lewis et al. (1984) reported that turbulent-induced mixing impacts the algal photosynthetic rate. Meanwhile, frontal instability processes can also impact phytoplankton productivity. The scales are 0.1–10 km horizontally and 10–100 m vertically comparable to the baroclinic Rossby radius and mixed-layer depth, and hours–days comparable to the inertial period (Capet et al., 2008; McWilliams, 2016). The timescale on which submesoscale processes transport oceanic properties and tracers are comparable to those of the phytoplankton growth (Mahadevan, 2016). Submesoscale instabilities can overcome large-scale balances (Molemaker et al., 2005), generating vertical motion and enhanced mixing in localized regions near the sea surface, as revealed by studies using submesoscale-resolving models (Freilich & Mahadevan, 2021; Mahadevan, 2006) and in situ drifters (Tarry et al., 2021). Therefore, intense upwelling can be induced by submesoscale frontal instabilities, such as symmetric instability (SI, Bachman et al., 2017; Brannigan, 2016; Thomas et al., 2013) and mixed-layer baroclinic instability (BCI, Boccaletti et al., 2007; Fox-Kemper et al., 2008). Upwelling in fronts can bring nutrients into the euphotic zone, which can cause intermittent blooms (Levy et al., 2012; Mahadevan, 2016). Frontal instabilities also lead to restratification of the near-surface layer (Bachman et al., 2017; Boccaletti et al., 2007; Haine & Marshall, 1998), trapping nutrients and phytoplankton cells in the euphotic zone, increasing mean light exposure, and triggering blooms (Mahadevan et al., 2012; Taylor & Ferrari, 2011a).

In this study, we analyzed physical and biological parameters using observational and model data. The results suggest that instability-related restratification near the coastal front plays a significant role in the off-coast blooming during NE wind relaxation in the northern TWS.

2. Materials and Methods

2.1. Field Investigation and Cruise Observation

Seven in situ cruises were carried out in the northern TWS study area (Figure 1b) in February 2012 April 2014, March 2015 November 2015, March 2016 March 2018, and March 2019 (i.e., winter and early spring). They were sponsored by Natural Science Foundation of China (NSFC), and served by R/V Yanping No. 2. The cruise in March 2019 was high-resolution and others were low-resolution, with their cross-shore section spatial resolutions of roughly 3 and 20 km, respectively. Sea conditions were severe and dangerous under strong sustained NE wind. Consequently, only one cruise was carried out during a persistent NE wind. Additionally, only one cruise was conducted during a persistent SW wind, due to the scarce wind condition in the winter and spring TWS. The other five cruises were conducted during the NE wind relaxation period.

A total of 54 hydro-cast stations were located along nine cross-shore transects near China's mainland coast (red dots in Figure 1b), including seven low-resolution and two high-resolution sections. Hydrographic data were collected at each station using Sea-Bird® SBE917plus CTD. The measurement accuracy (i.e., the correctness) of temperature, conductivity, and pressure sensors are 0.001°C, 0.0003 S m^{-1}, and 1 dbar, respectively. The measurement resolution (i.e., the least significant digit) of temperature, conductivity, and pressure sensors are 0.0002°C, 0.00004 S m^{-1}, and 0.68 dbar, respectively. According to the specifications for oceanographic survey from National Standardization of the P. R. China (GB/T 12763.2–2007, Tang et al., 2007), measurements of the downward CTD casts were derived as the in situ data. After the process of quality control (e.g., bad data erasing, zero pressure correction, adverse pressure data processing, etc.), the in situ data were chosen or linearly interpolated at the standard observation depths (as shown in Figures 2–5).

For the low-resolution cruises, seawater samples were collected at the standard depths of each station and analyzed for nutrients and Chl-a. Nitrate analysis was conducted employing a copper–cadmium reduction method

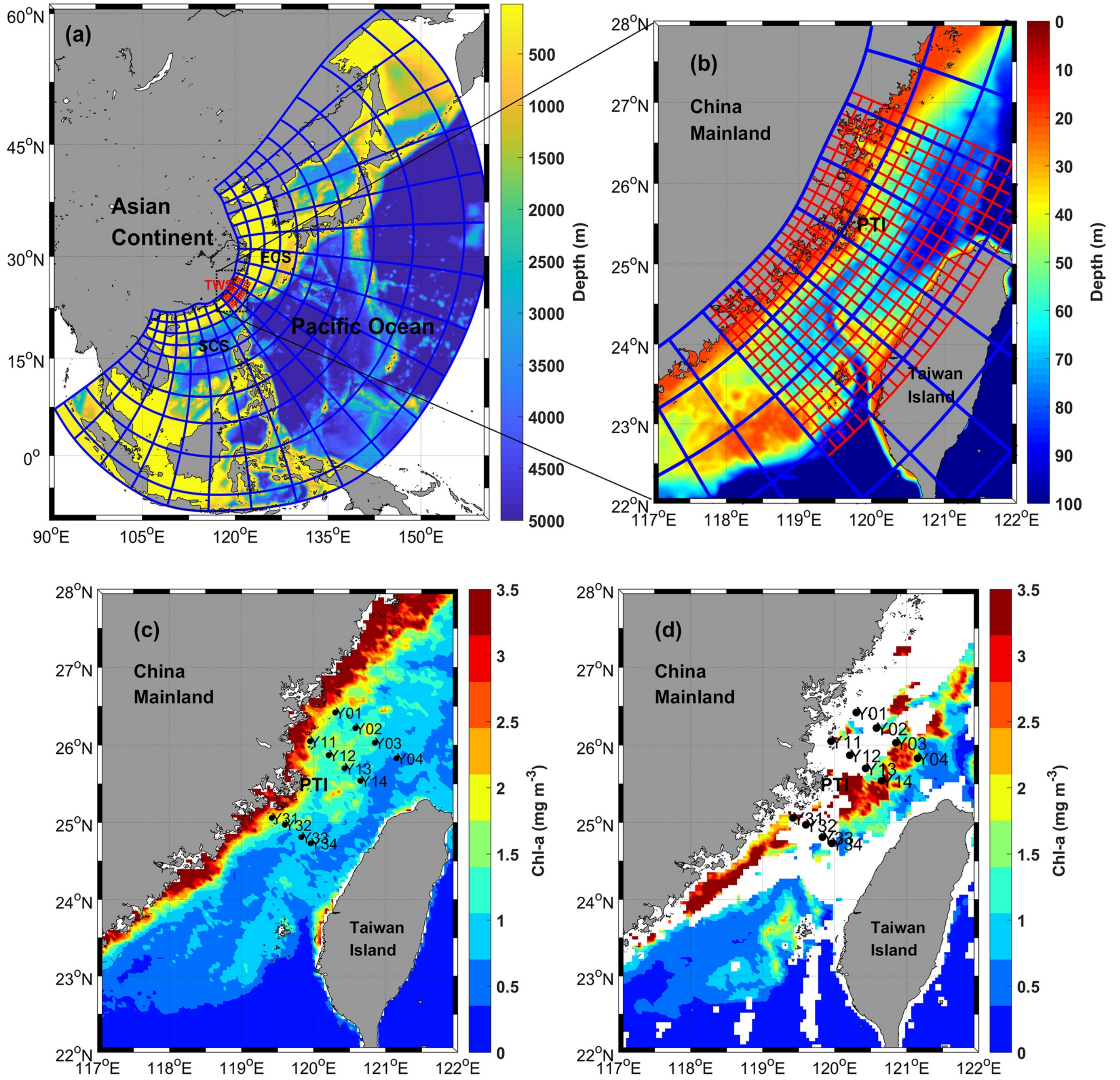

Figure 2. (a) Nesting model domain of the parent (blue) and child (red) grids with a nesting scale of 5, and the bottom topography (color shading), the dashed black box shows the location of the zoomed-in view (b). ECS, SCS, and TWS denote the East China Sea, South China Sea, and Taiwan Strait, respectively. (b) The parent (blue) and child (red) grids with one line per 30 real grids, and bottom topography (color shading) in the TWS. PTI denotes the Pingtan Island. Composite maps of the OC-CCI sea-surface Chl-a in March and April from 1998 to 2018 (c), and from 31 March to 4 April 2015 (d). Cruise stations in late March of 2015 are presented as black dots.

(Hydes & Hill, 1985) using a Bran + Luebbe® QUAATRO continuous-flow analyzer (Dafner, 2015) with a detection limit of 0.03 μmolN L^{-1}. Chl-a was determined with seawater samples via high-performance liquid chromatography (HPLC, Bidigare et al., 1985), with a Dionex® UltiMate 3000 HPLC employed, with a detection limit of 0.01 mg m^{-3}. It was also measured directly by Seapoint® Chlorophyll Fluorometer carried on CTD via fluorometric method (Welschmeyer, 1994), with a detection limit of 0.02 mg m^{-3}. Generally, measurements of oceanic Chl-a by the two methods present similar patterns, with values of fluorometric Chl-a relatively higher than HPLC Chl-a (Bianchi et al., 1995). As the fluorometric method can be influenced by Chl-b and Chl-c, Bianchi et al. (1995) suggested HPLC as a routine technique for analyzing Chl-a in both continental margin and open ocean systems. Consequently, Chl-a measurements via HPLC were employed for the low-resolution cruises. In contrast, in situ data of HPLC Chl-a and nitrate measured with seawater samples were not available for the high-resolution cruise because of the sampling time constraint. Therefore, Chl-a data measured via fluorometric method were used instead for the high-resolution cruises in this study.

2.2. Satellite Data Analysis

Remote sensing of daily sea-surface Chl-a was obtained from the Ocean Color Climate Change Initiative (OC-CCI, https://esa-oceancolour-cci.org/) project of the European Space Agency. The data set is from September 1997, to December 2018, with a spatial resolution of 4 by 4 km. Zhang et al. (2006) and Hong, Liu, et al. (2011b) demonstrated that the sea-surface Chl-a in the TWS derived from satellite data are consistent with the concurrent field observations, except in turbid coastal waters.

2.3. Wind Data

Sea-surface wind data taken at 6-hr intervals from 1998 to 2018 were obtained from the National Centers for Environmental Predictions (NCEP)-DOE Reanalysis 2 data set (Kanamitsu et al., 2002). The spatial resolution is approximately 1.9° by 1.9° in the study area. NCEP wind data over the cruise stations in the northern TWS (dashed blue box in Figure 1b) were extracted for the analyses. Meanwhile, time series of the observational wind data at 1-hr interval in 2009 were collected from two buoys (blue diamond Figure 1b). The NCEP and observed wind vectors were projected in the along-shore direction (double-headed arrow in Figure 1b) to extract the NE wind component. Figures 1c and 1d demonstrate that the correlation coefficients between the daily running-mean NCEP NE wind (blue line) and the observed NE wind (red line) can reach 0.88 (Figures 1c) and 0.86 (Figure 1d), with relatively low Root-Mean-Square Error (RMSE) of 4.15 and 3.44 m s^{-1}, at wind observation Buoys A and B from 25 February to 31 December 2009, respectively. It shows that the NCEP wind data have sufficient accuracy across the TWS (Kuang et al., 2015), and can be used for further analyses. Note that the daily running-mean NCEP wind was used to remove the signal of high-frequency (i.e., hourly) variations. It also proves that the prevailing winds in the TWS are spatially homogeneous, particularly during the NE monsoon period (Hong, Chai, et al., 2011; Hu et al., 2010).

2.4. Sea-Surface Temperature Data

Daily Optimum Interpolation sea-surface temperature (OISST, Huang et al., 2021) data from 1998 to 2018 were obtained from NOAA Physical Sciences Laboratory (PSL, https://psl.noaa.gov/data/gridded/data.noaa.oisst.v2.highres.html). It has a spatial resolution of 0.25° by 0.25° in the study area. OISST has the advantage of being available from 1998 to 2018. It can be used to reasonably derive the location and spatiotemporal variations of the front in the TWS, although it has relatively coarse resolution and may underestimate of the front intensity. Similarly, Koseki et al. (2019) employed the OISST to study the frontogenesis of the Angola-Benguela Frontal Zone in the mixed layer; Oey et al. (2013) also used the OISST to reflect the spatial characteristics of the warming trend in the TWS.

2.5. Diagnostic Methods

The buoyancy (b) and buoyancy frequency (N^2) are:

$$b = -(g\rho/\rho_0), \tag{1}$$

$$N^2 \equiv b_z = -(g\rho_z/\rho_0), \tag{2}$$

where g is the acceleration due to gravity (9.8 m·s^{-2}), ρ the potential density, ρ_0 the reference density (1,025 kg·m^{-3}), z the vertical coordinate, and subscript "z"denotes partial differentiation.

The Ekman layer depth (D_E) can be written mathematically using the classical Ekman theory calculation (Stewart, 2008):

$$D_E = (\pi\rho_{\text{air}}U_{\text{wind}}C_d) \Big/ \left(0.0127\rho_0\Omega\sqrt{2\sin\varphi}\right), \tag{3}$$

where ρ_{air} denotes the air density (1.3 kg·m^{-3}); U_{wind}, wind speed; C_d, the drag coefficient; $\boldsymbol{\Omega}$, Earth's angular velocity $\left(7.3 \times 10^{-5}\ \mathrm{rad} \cdot \mathrm{s}^{-1}\right)$; and φ, local latitude (26°N in the northern TWS).

The instability-induced eddy-driven overturning stream function (ψ_e) can be parameterized as follows (Fox-Kemper et al., 2008):

$$\psi_{\mathrm{e}} = 0.06 H^2 b_{\mathrm{x}} / f, \tag{4}$$

where H denotes the ML depth. It is estimated as the depth of the lighter CCC on the nearshore side of the along-shore front in the TWS. b_x is the near-surface front intensity, x denotes the cross-shore coordinate, and subscript "x" denotes partial differentiation; and f denotes the Coriolis frequency.

The classical Ekman scaling of the wind-induced mean overturning stream function (ψ_w) is as follows:

$$\psi_w = -\tau / \rho_0 f, \tag{5}$$

where τ denotes the surface wind stress.

Consequently, the ratio (r) of eddy-driven and wind-driven buoyancy fluxes can be estimated as follows (Mahadevan et al., 2010, 2012):

$$r = \psi_w / \psi_e = -\tau / \left(0.06 \rho_0 b_x H^2\right). \tag{6}$$

The positive and negative values of the ratio r denote the effects of down-front and up-front winds, respectively. If the absolute value of the ratio r is smaller than 1, the eddy-driven buoyancy flux is dominating, suggesting near-surface restratification mainly induced by frontal instabilities (Bachman et al., 2017; Boccaletti et al., 2007; Haine & Marshall, 1998); In contrast, if the absolute value of the ratio r is larger than 1, the wind-driven buoyancy flux is dominating. At this time, down-front wind drives destratification of the water column (Thomas & Lee, 2005), while up-front wind lead to restratification near the Ekman depth (Chang & Oey, 2011).

SI begins when there is negative Ertel potential vorticity (PV) near the frontal region in the northern hemisphere (Hoskins, 1974). PV is formulated as follows:

$$\mathrm{PV} = \zeta_{\mathrm{a}} \cdot \nabla b, \tag{7}$$

where $\zeta_a = \left(\mathrm{f}\mathbf{k} + \nabla \times \vec{\mathbf{u}}\right)$ is the absolute vorticity. $\mathbf{k}$, unit vector in the vertical direction; ∇, three-dimensional Hamiltonian operator; $\vec{\mathbf{u}} = (u, v, w)$, three-dimensional velocity. ∇b is the spatial derivative of buoyancy, denoting the front intensity. Hence, one can visualize the "opening" of the angle between ζ_{a} and b_{x} from an initially zero value to π/2 as the down-front wind forces an increasingly stronger front. SI acts to restore the fluid back to a marginally stable state, that is, $PV = 0$, by effectively mixing in a fluid of higher PV from surrounding waters (Bachman & Taylor, 2014; Bachman et al., 2017). Note that restratification by SI is effective but minimal once PV reaches zero (Bachman et al., 2017), and the SI-neutral state can still be unstable to other forms of instability such as BCI (Haine & Marshall, 1998).

The balanced Richardson number (Ri_b) can be used as another criterion for the development of SI and BCI. It can be written as (Thomas et al., 2013):

$$Ri_{\mathrm{b}} = f^2 N^2 / \nabla_h b^2, \tag{8}$$

where ∇_h denotes the two-dimensional Hamiltonian operator in the horizontal direction, which can be estimated as b_{x} in the TWS. A series of previous studies have shown that SI occurs when $0.25 \leq Ri_b \leq 0.95$, which is equivalent to negative PV in the northern hemisphere (Stone, 1966, 1970). Meanwhile, the SI-unstable state is also unstable to the frontal BCI, for that BCI can develop even when $Ri_b > 1$ (Boccaletti et al., 2007).

The BCI-induced eddy energy evolution can be described based on the instability energy equation (Equations s7 and s8 in Supporting Information S1). BC is the baroclinic conversion term (Equation 9). If it is positive, energy is drained from mean potential energy to eddy potential energy (EPE, Equation 10); PKC is the buoyancy flux conversion term (Equation 11). If it is positive, it extracts energy from EPE to eddy kinetic energy (EKE, Equation 12). These terms per unit mass can be expressed as (Oey, 2008; Orlanski & Cox, 1972):

$$\mathrm{BC} = -g^2 \left[\overline{u'\rho'}\left(\overline{\rho}\right)_{\mathrm{x}} + \overline{v'\rho'}\left(\overline{\rho}\right)_y\right] / \left(\rho_0^2 N^2\right). \tag{9}$$

$$\mathrm{EPE} = g^2\overline{\rho'^2}/\left(2\rho_0^2 N^2\right). \tag{10}$$

$$\mathrm{PKC} = -g\overline{\rho' w'}/\rho_0. \tag{11}$$

$$\mathrm{EKE} = \left(\overline{u'^2} + \overline{v'^2}\right)/2. \tag{12}$$

Contributions of the mean (mean term) and eddy (perturbation term) buoyancy advections to the temporal evolution rate of N^2 can be expressed as follows (Mahadevan et al., 2010; Taylor & Ferrari, 2010):

$$\left(N^2\right)_t = -\overbrace{\left[\bar{u}\left(\bar{b}\right)_x + \bar{v}\left(\bar{b}\right)_y + \bar{w}\left(\bar{b}\right)_z\right]_z}^{\text{Mean}} - \overbrace{\left[\left(\overline{u'b'}\right)_x + \left(\overline{v'b'}\right)_y + \left(\overline{w'b'}\right)_z\right]_z}^{\text{Perturbation}} + \overbrace{\left[\left[B^z\left(\bar{b}\right)_z\right]_z\right]_z}^{\text{Diffusion}}, \tag{13}$$

where subscript "t" denotes temporal differentiation. B^z is the vertical turbulent diffusion coefficient. The eddy buoyancy advection is mainly driven by the submesoscale instability processes, while the mean buoyancy advection is associated with larger-scale processes such as Ekman transport and geostrophic adjustment. Note that lighter water flowing above denser water leads to a positive buoyancy advection.

Contributions of physical and biological processes on the temporal variation rate of Chl-a can be expressed as follows (Wang et al., 2016):

$$\begin{aligned}\left(\overline{\mathrm{Chl}}\right)_t = &-\overbrace{\left[\bar{u}\left(\overline{\mathrm{Chl}}\right)_x + \bar{v}\left(\overline{\mathrm{Chl}}\right)_y + \bar{w}\left(\overline{\mathrm{Chl}}\right)_z\right]}^{\text{MeanAdv}} - \overbrace{\left[\left(\overline{u'\mathrm{Chl}'}\right)_x + \left(\overline{v'\mathrm{Chl}'}\right)_y + \left(\overline{w'\mathrm{Chl}'}\right)_z\right]}^{\text{PerturbationAdv}} \\ &+ \overbrace{\left[B^z\left(\overline{\mathrm{Chl}}\right)_z\right]_z}^{\text{Diffusion}} + \overbrace{\overbrace{\mu\overline{\mathrm{Chl}}}^{\text{Growth}} \overbrace{-g\overline{\mathrm{Zoo}}}^{\text{Grazing}} \overbrace{-m\overline{\mathrm{Chl}}}^{\text{Mortality}} \overbrace{-\tau\overline{\mathrm{Chl}}}^{\text{Aggregation}} \overbrace{-w_p\left(\overline{\mathrm{Chl}}\right)_z}^{\text{Sinking}}}^{\text{Bio}}.\end{aligned} \tag{14}$$

Chl and Zoo denote Chl-a and zooplankton concentration, respectively. Physical process includes advection and diffusion. The advection process includes mean (MeanAdv) and perturbation (PerturbationAdv) advections, which are primarily driven by the larger-scale and submesoscale processes, respectively. The diffusion process is dominated by vertical diffusion with horizontal diffusion negligible. Biological process (Bio) includes phytoplankton growth (μ denotes the growth rate), zooplankton grazing (g denotes the grazing rate), phytoplankton mortality (m denotes the mortality rate), aggregation (τ denotes the aggregation rate), and sinking (w_p denotes the sinking velocity).

In the above equations, overbar denotes a 3-day averaging operator according to the spatiotemporal scale of the instability, and prime denotes the deviation from this average.

2.6. Self-Organizing Map Analysis

We employed the self-organizing map (SOM; Kohonen, 1998, 2013) method to analyze the cruise and satellite observational data. The SOM is based on an unsupervised learning neural network and effectively identifies and classifies features in data (Liu et al., 2006; Lu et al., 2019). It extracts data features through mapping high-dimensional input data onto a low dimensional (usually two-dimensional) space. It preserves the information of the input data by keeping their topological relationships. Liu et al. (2006), Reusch et al. (2005) demonstrated that the SOM could be more effective than the more traditional empirical orthogonal function method for feature extraction, especially highly nonlinear signals. Therefore, this method is widely used in oceanography (Gu et al., 2018; Liu & Weisberg, 2011; Solidoro et al., 2007; Yin et al., 2014; Zeng et al., 2015, etc.). In this study, we define the map size as three-by-one to represent the features of Chl-a distribution in the TWS during NE wind (Type I), NE wind relaxation (Type II), and SW wind (Type III).

2.7. High-Resolution Model Configurations

2.7.1. Physical Model

A High-resolution physical–biological model was applied to reproduce off-coast bloom in the TWS. The physical model is an updated version of the Taiwan Strait Nowcast/Forecast System (TFOR), a robust operational ocean model of the TWS (Chen et al., 2014; Liao et al., 2013; Lin et al., 2016; Lu et al., 2015; ; Wang et al., 2013, 2016). It is based on the Regional Ocean Modeling System (ROMS, Shchepetkin & McWilliams, 2003, 2005), a free-surface, terrain-following, primitive equation ocean circulation model under hydrostatic and Boussinesq assumptions. The modeling domain covers the northwestern Pacific Ocean using curvilinear-orthogonal grids, with a horizontal resolution of nearly 3 km in the TWS (blue grid in Figure 2b). A child grid was nested with a nesting scale of 5, leading to a horizontal resolution of about 0.6 km in the TWS (red grid in Figure 2b). 30 vertical layers were derived using a stretching function, where $\theta_s = 3.0$, $\theta_b = 0.4$, and $h_c = 10\,\mathrm{m}$ following the S-coordinate scheme (Song & Haidvogel, 1994). The model bathymetry was obtained by combining 25 digitized ocean charts from the Maritime Safety Administration (China), the 0.5' gridded bathymetry of the TWS (http://www.odb.ntu.edu.tw), and the ETOPO2v2 data published by the National Geophysical Data Center at the National Oceanic and Atmospheric Administration (NOAA, https://www.ngdc.noaa.gov). A weak filter (rfact = 0.35) was applied to smooth the bathymetry to reduce the unexpected diapycnal mixing error.

The model used the centered fourth-order advection scheme for momentum and tracers. The model used Smagorinsky algorithm to parameterize the horizontal turbulent mixing (Smagorinsky, 1963), and the Mellor–Yamada level 2.5 turbulence scheme to parameterize the vertical turbulent mixing (Mellor & Yamada, 1982), with the background vertical viscosity and diffusion coefficients set to 10^{-5} and 10^{-6} $\mathrm{m}^2\ \mathrm{s}^{-1}$, respectively. Chapman (Chapman, 1985) boundary conditions were used for free surfaces, Flather boundary conditions (Flather, 1976) were used for two-dimensional momentum, and clamped boundary conditions were employed for three-dimensional momentum and tracers. The initial fields and lateral open boundary conditions, including sea level, velocity, temperature, and salinity, were obtained from MyOcean data (http://marine.copernicus.eu/servicesportfolio/access-to-products/). Tidal forcing with 10 main tidal components (M_2, S_2, N_2, K_2, K_1, O_1, P_1, Q_1, M_f, and M_m) was provided by TPXO7.0 (Egbert & Erofeeva, 2002) at the lateral boundary. The monthly mean discharges of the major rivers along the mainland coast were also included in the model, with their salinities set to zero. The air-sea fluxes, including momentum flux, heat flux, and freshwater flux, were interpolated from the National Centers for Environmental Prediction data (NCEP, https://data.nodc.noaa.gov/ncep/). Moreover, the sea-surface net heat flux was justified by nudging the referenced sea-surface temperature with a modest relaxation coefficient to improve the modeling performance of temperature (Zhao et al., 2020). Other details on the settings and evaluations of the physical model can be found in Lin et al. (2016).

2.7.2. Biological Model

The physical model was coupled with a nitrogen-based nutrient–phytoplankton–zooplankton–detritus biological model (Fennel et al., 2006). The biological model solves for nitrate, ammonium, phytoplankton, Chl-a, zooplankton, small detritus, and large detritus. Following Geider et al. (1996, 1997), it accounts for the change in Chl-a content per phytoplankton cell relative to changes in light and nutrient conditions. The model separates new and regenerative productivity processes by nitrate and ammonium. The model also accounts for the inhibition of nitrate uptake by ammonium. It groups detritus according to size into large and small components. Small detritus resulting from phytoplankton mortality and inefficient zooplankton ingestion can aggregate to form large detritus. A fraction of the detritus mineralizes into ammonium, and the remaining sinks to the seabed.

The initial fields and the lateral open boundary conditions of the nitrate concentration and Chl-a were obtained from the World Ocean Atlas (WOA)-2005 (https://www.ncei.noaa.gov/products/world-ocean-atlas) and SeaWiFS data sets (http://oceancolor.gsfc.nasa.gov/), respectively. The Chl-a vertical profile in the euphotic layer was extrapolated from the SeaWiFS sea-surface Chl-a (Morel & Berthon, 1989). Chl-a below the euphotic depth was set to 0.02 mg m^{-3}. The initial fields and the lateral open boundary conditions of the phytoplankton and zooplankton concentrations were set as half and one fifth of the Chl-a (Liu et al., 2002). Other details on the settings and evaluations of the biological model can be found in Wang et al. (2016).

As presented in Figures 2c and 2d, off-coast phytoplankton bloom north of the PTI was observed by satellite in late March of 2015, with significantly high Chl-a extending near 100 km off the mainland coast. The off-coast Chl-a reached 3.5 mg m^{-3} (Figure 2d) while its climatological value (21-year composite) is below 2.0 mg m^{-3} (Figure 2c). To reproduce this bloom, the physical–biological model was hot-started from its restart file on 1 January 2014 with the parent grid. Subsequently, the child grid was nested with the parent grid on 1 March 2015, and conducted to 10 April 2015.

3. Observation and Model Results

3.1. Low-Resolution Cruise Results

We classify the low-resolution cruise observations into three groups based on the dominant wind direction: NE wind (Section 3.1.1), SW wind (Section 3.1.2), and NE wind relaxation (Section 3.1.3). We define off-coast bloom as when the surface to 20-m averaged Chl-a reaches or exceeds 0.6 mg m^{-3}.

3.1.1. NE Wind

Figure 3 shows the density, Chl-a, nitrate concentration, and N^2 at cruise sections Y3, Y2, and Y1 (panel n) in February 2012. Note that we conducted the cruise at Y3 first, then Y2 and Y1, as indicated in the wind time series (panel m). The wind was predominantly NE during this cruise. It was weak SW before the cruises. However, it became NE during Y3 and Y2, and strengthened to more than 10 m s^{-1} before weakening during Y1. Observation

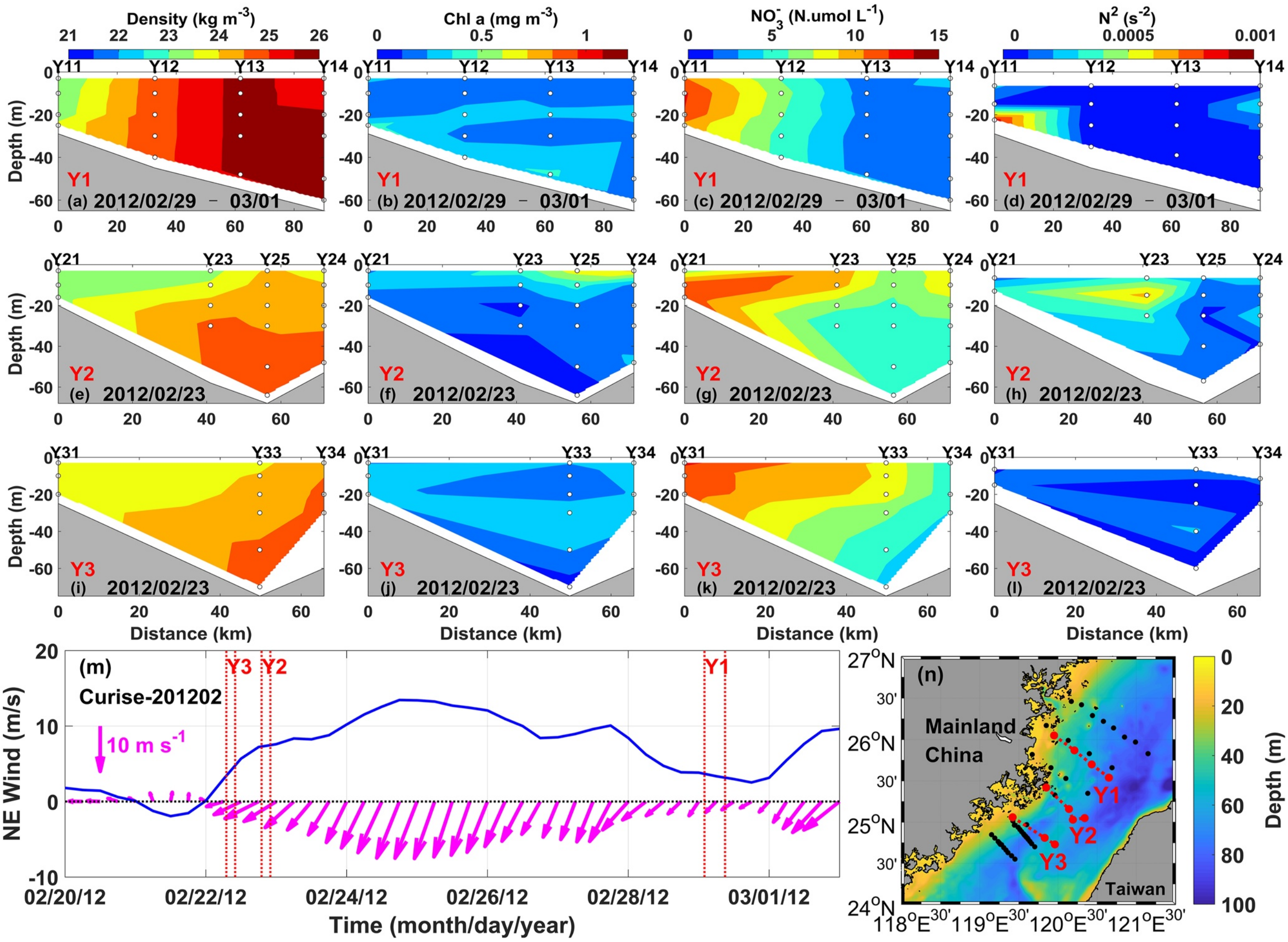

Figure 3. Cross-shore density (a, e, i), HPLC Chl-a (b, f, j), nitrate concentration (c, g, k), and buoyancy frequency (d, h, l) at sections Y1, Y2, and Y3 (see map inset in n). Observation stations are labeled across the top, and white dots indicate the sample points for each station. (m) Time series of wind vectors (magenta arrows) and the along-shore component (blue line) over the stations (dashed blue box in Figure 1b) in late February of 2012. Red dashed lines indicate cruise times for each section.

shows that the lighter and eutrophic CCC flowed within the western part of the sections, whereas the denser and oligotrophic SMC occupied the eastern part. Cross-shore nitrate presented spatial similarity to density, suggesting distinctive physical–biological characteristics of the two water masses. Along-shore front was formed where the two water masses converged (Hong, Chai, et al., 2011; Hu et al., 2010). Under the down-front NE wind, the density exhibited vertical homogeneity (Figures 3a, 3e and 3i) with tilted isopycnals and weak stratification near the surface (small N^2, Figures 3d, 3h, and 3l).

As a result, Chl-a was low in this NE wind series (Figures 3b, 3f and 3j). For sections Y1, Y2, and Y3, the surface 20-m averaged Chl-a was 0.21, 0.29, and 0.24 mg m^{-3}, respectively. Therefore, phytoplankton did not bloom.

Fronts at sections Y2 and Y3 were located further offshore compared with Y1. This might be because the cruises at sections Y2 and Y3 were conducted several days before Y1, during which a strong down-front NE wind persisted over the strait (Figure 3m). Another possible reason is that sections Y2 and Y3 are located nearshore off the PTI (Figure 1b), where the CCC tends to separate from the mainland due to topography (Liao et al., 2013; Wang et al., 2016). Moreover, although the NE wind relaxed before the cruise along section Y1 (25–29 February), the winds sustained relatively high speeds of about 5 m·s^{-1}.

3.1.2. SW Wind

Figure 4 presents cross-shore physical–biological observations at sections MC, MB, and MA (panel n) in April 2014. Wind time series (panel m) shows an up-front SW wind of approximately 5 m·s^{-1} persisted for nearly

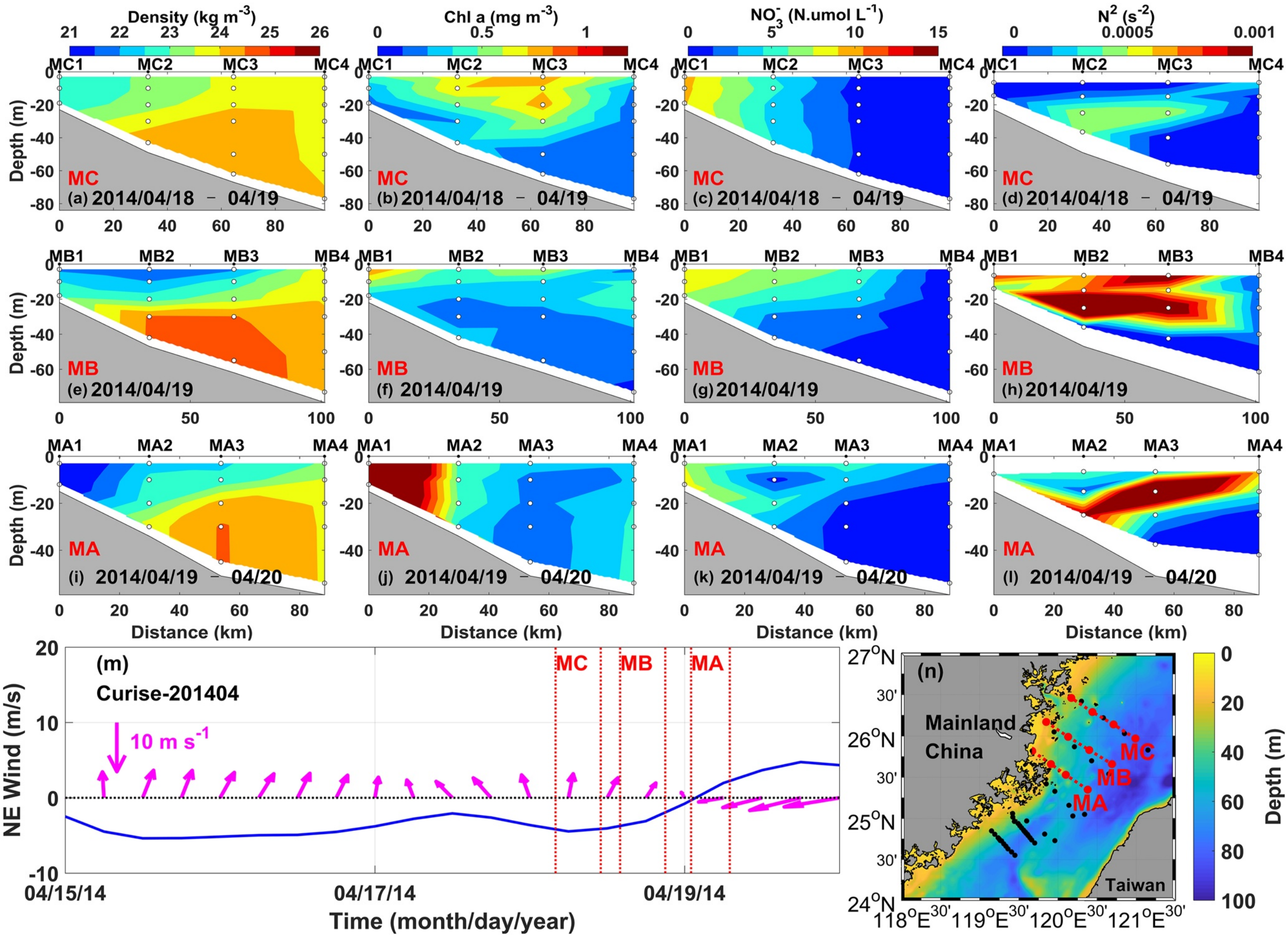

Figure 4. Cross-shore density (a, e, i), HPLC Chl-a (b, f, j), nitrate concentration (c, g, k), and buoyancy frequency (d, h, l) at sections MC, MB, and MA (see map inset in n). Observation stations are labeled across the top, and white dots indicate the sample points for each station. (m) Time series of wind vectors (magenta arrows) and the along-shore component (blue line) over the stations (dashed blue box in Figure 1b) in middle April of 2014. Red dashed lines indicate cruise times for each section.

4 days before this cruise, and was relaxing to zero during this cruise. Along-shore density and nutrient front also existed in this SW wind series. However, flatter isopycnals (Figures 4a, 4e and 4i) with intense stratification (high N^2, Figures 4d, 4h, and 4l) near the 20-m depth were observed under the up-front SW wind. With U_{wind} equaling 4 m·s^{-1} (Figure 4m) and C_d equaling 0.0012, the estimated Ekman layer depth D_E is 22 m. Therefore, the intense stratification developed near the Ekman layer depth, closely related to the Ekman effect of the up-front wind.

This SW wind series also had low Chl-a (Figures 4b, 4f and 4j). For sections MC, MB, and MA, the surface 20-m averaged Chl-a was 0.55, 0.39, and 0.35 mg m^{-3}, respectively. Therefore, phytoplankton blooms did not occur. Note that the anomalously high Chl-a near station MA1 was removed from the analysis (Figure 4j). This station is located too nearshore (nearly 10 km, Figure 4n) to be considered as an off-coast bloom. Unlike the NE wind series, the cross-shore nitrate in the SW wind series did not correlate strongly with density, with higher nitrate concentrations inshore relative to the fresher water (Figures 4c, 4g and 4k). The different patterns of nitrate and density indicate that the water mass theory cannot fully explain the transportation and distribution of nutrients (e.g., nitrate) in the TWS. Other physical processes which likely play a role are described in the following Sections.

3.1.3. NE Wind Relaxation

Off-coast phytoplankton blooms occurred during each of the low-resolution cruises that took place during the NE wind relaxation periods: March 2015 November 2015, March 2016, and March 2018. Typical cruise in late March of 2015 are presented in this sub-Section.

Figure 5 presents cross-shore observations at sections Y0, Y1, and Y3 (panel n) in late March of 2015. Wind time series (panel m) shows a strong NE wind of nearly 10 m·s^{-1} was relaxing to zero roughly 1 day before this cruise, and became SW wind of 3–4 m·s^{-1} during this cruise. Near the off-coast frontal region, intense near-surface stratification of high N^2 (less than 10-m depth, e.g., Figure 5d) was observed during this cruise.

With the development of surface stratification, off-coast phytoplankton bloom occurred during this cruise, with the surface 20-m averaged Chl-a being 0.89, 0.88, and 0.82 mg m^{-3} for sections Y0, Y1, and Y3, respectively (Figures 5b, 5f and 5j). High Chl-a of nearly 1.2 mg·m^{-3} (Figures 5b and 5f) was correlated with low nitrate concentration (Figures 5c and 5g) near stations Y03 and Y13, suggesting the consumption of nutrients by phytoplankton growth.

On the other hand, observations indicated nearshore nitrate appeared to be transported toward the offshore upper layer, especially near the pycnocline (e.g., Figures 5c and 5g). This process provided sufficient nutrients for near-surface phytoplankton growth, conducive to the bloom development. Note also that nitrate and density exhibited similar cross-shore patterns in this NE wind relaxation series, as observed in the NE wind series.

Cruises conducted in November 2015 March 2016, and March 2018 demonstrated similar off-coast bloom processes as in March 2015, as presented in Figures S1, S2, and S3 in Supporting Information S1, respectively.

3.1.4. Composite and SOM Analyses

Composite analysis was conducted using the cross-shore observations from the six low-resolution cruises to extract the characteristic patterns under different wind series in the TWS. The 18 sectional patterns were first interpolated to the terrain-following sigma coordinate (Shchepetkin & McWilliams, 2005). Note that sigma levels of 0 and −1 denote the near-surface and near-bottom depths of available in situ data, respectively. As shown in Figure 6, composite patterns during NE and SW wind both exhibit low off-coast Chl-a (Figures 6b and 6j), with weak stratification under NE wind (Figure 6a, as in Section 3.1.1) and intense stratification near the Ekman layer under SW wind (Figure 6i, as in Section 3.1.2). In contrast, composite pattern during NE wind relaxation shows off-coast bloom, with the surface 20-m averaged Chl-a reaching 0.84 mg m^{-3} (Figure 6f). It is worthy to note that the bloom occurs with along-isopycnal nutrient supplement (Figures 6e and 6g) and intense near-surface stratification (Figure 6h) near the frontal region, as aforementioned in Section 3.1.3.

SOM analysis was also conducted using the cross-shore Chl-a observations from the six low-resolution cruises. The 18 sectional Chl-a patterns on the sigma coordinate were arranged in a three-by-one SOM array to obtain three characteristic types (Figure S4 in Supporting Information S1). The SOM patterns are consistent with the composite patterns, with Type I (Figure S4 in Supporting Information S1, row 1), II (Figure S4 in Supporting Information S1, row 2), and III (Figure S4 in Supporting Information S1, row 3) similar to composites of NE wind

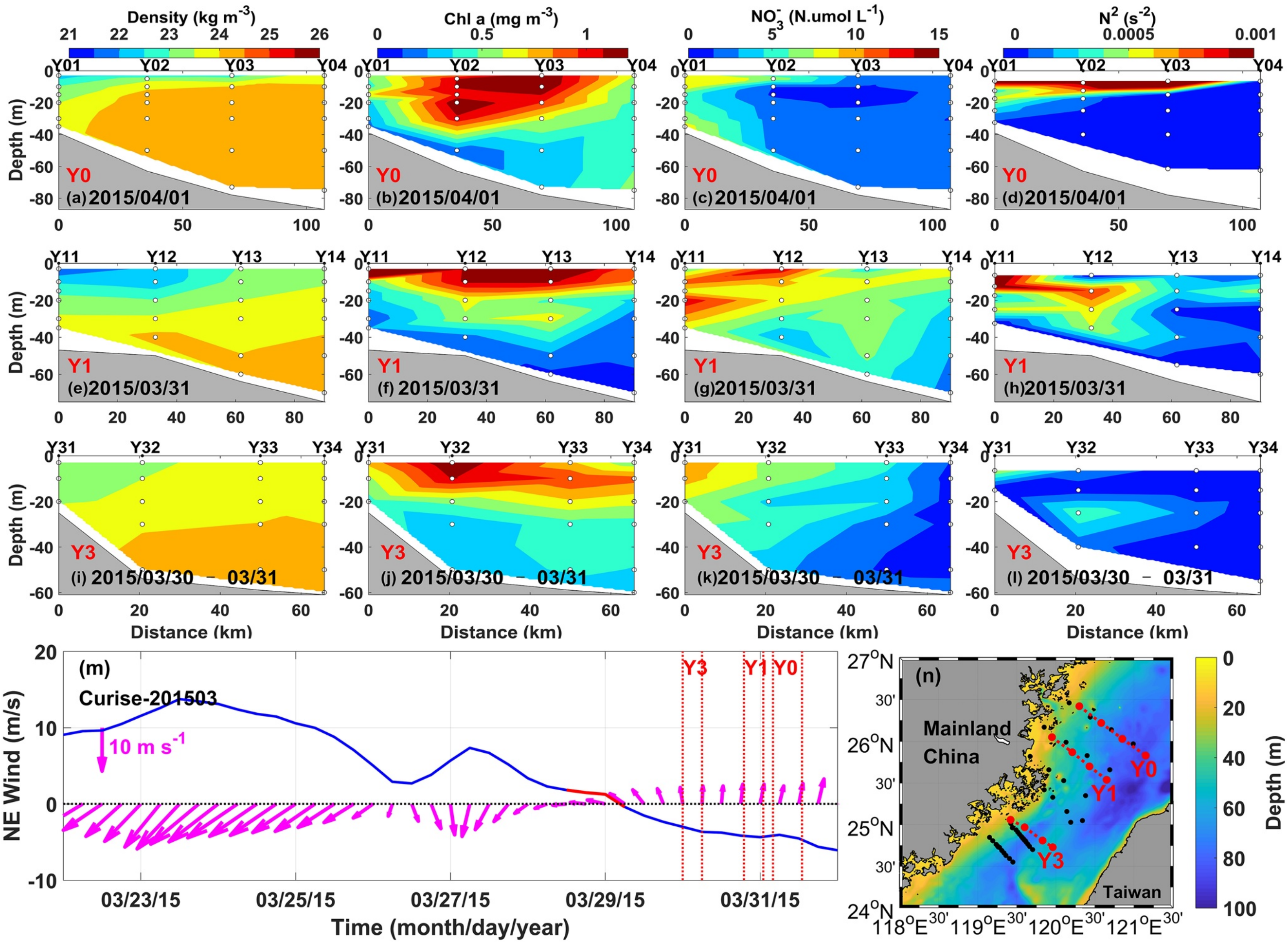

Figure 5. Cross-shore density (a, e, i), high-performance liquid chromatography (HPLC) Chl-a (b, f, j), nitrate concentration (c, g, k), and buoyancy frequency (d, h, l) at sections Y0, Y1, and Y3 (see map inset in n). Observation stations are labeled across the top, and white dots indicate the sample points for each station. (m) Time series of wind vectors (magenta arrows) and the along-shore component (blue line) over the stations (dashed blue box in Figure 1b) in late March of 2015. The short red line in (m) indicates the identified NE relaxation event as in Section 3.4.

(Figure 6, row 1), NE wind relaxation (Figure 6, row 2), and SW wind (Figure 6, row 3), respectively. Among the 12 sections during NE wind relaxation period, 11 of them were grouped in Type II, demonstrating the pattern during off-coast bloom.

3.2. High-Resolution Cruise Results

An high-resolution cruise was also conducted during NE wind relaxation in March of 2019. The cross-shore observations at sections *G* and F are presented in Figure 7. Wind time series (panel i) shows a NE wind of nearly 10 m·s^{-1} was relaxing to zero several hours before this cruise, and then developed as a weak NE wind of 3–4 m·s^{-1} during this cruise. Along-shore density front was generated by the cold, fresh CCC and warm, saline SMC (Figure S5 in Supporting Information S1), whose fine structure was resolved with a spatial resolution of roughly 2–3 km (Figures 7a and 7e).

Off-coast bloom developed in the near-surface frontal region at section *G* (stations G9 and G11, Figure 7b). The near-surface Chl-a reaches 2.0 mg m^{-3} and the surface 20-m averaged Chl-a was nearly 1.1 mg m^{-3}. Note that the high Chl-a co-occurred with the intense near-surface stratification (Figure 7d). Figure 8a shows cross-shore Ri_b calculated using the high-resolution density at section G. The Ri_b was less than 1 near the frontal region with a horizontal length scale of ~5 km. It indicated the existence of submesoscale instabilities including SI and BCI. The near-surface stratification could only be driven by the restratification effect of instabilities under the

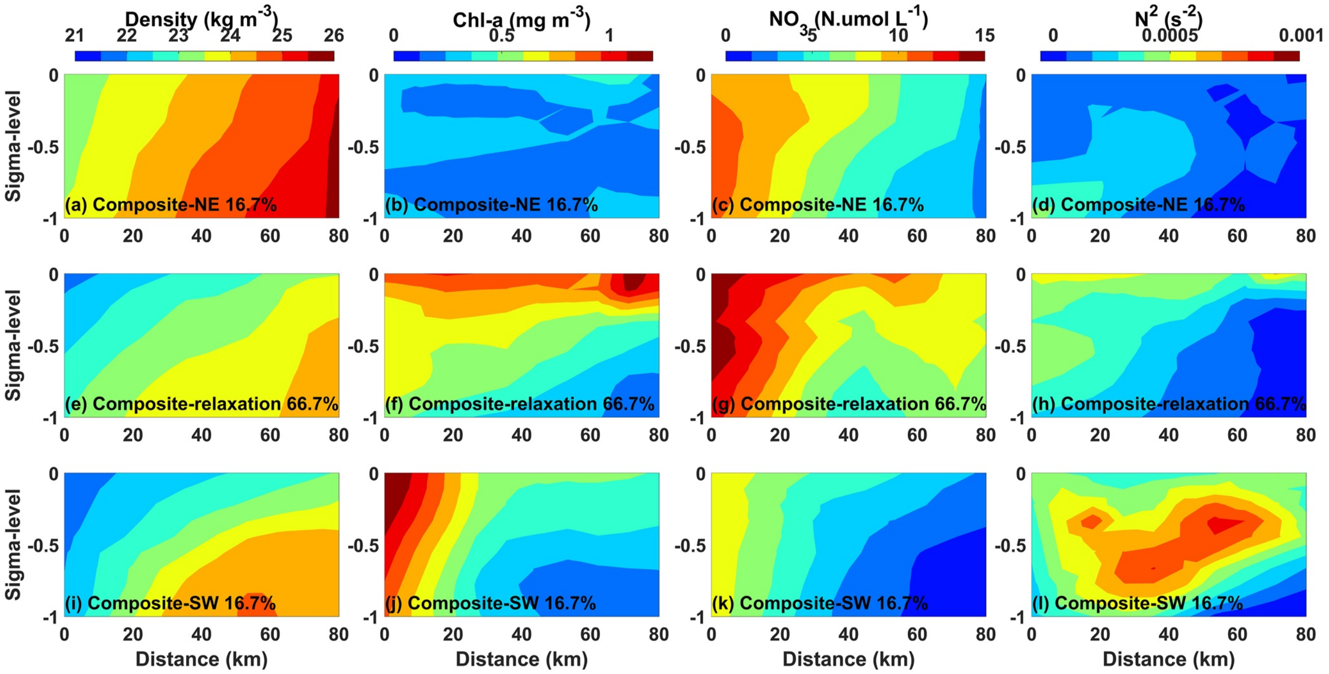

Figure 6. Composite patterns of sectional density (a, e, i), high-performance liquid chromatography (HPLC) Chl-a (b, f, j), nitrate concentration (c, g, k), and buoyancy frequency (d, h, l) for the low-resolution cruises during NE wind (row 1, including Figure 3), NE wind relaxation (row 2, including Figures 5, S1, S2, and S3 in Supporting Information S1), and SW wind (row 3, including Figure 4) on the vertical sigma coordinate.

down-front NE wind. With $b_x \sim -6.8 \times 10^{-7}$ s^{-2} and $H \sim 30$ m near stations G9 and G11, the down-front NE wind of ~4 m s^{-1} gives the r value of approximately 0.56. It indicates that restratification effect of instabilities was more vigorous compared with destratification effect of the down-front wind, triggering near-surface stratification and thus the off-coast bloom.

In contrast, near-surface stratification and off-coast bloom did not develop at section F (Figures 7e and 7f). High Chl-a distributed only in the near-shore subsurface 15-m layer (Figure 7f). Figure 8b also shows low cross-shore Ri_b near the frontal region of stations F5 and F6, suggesting the development of submesoscale instabilities with a horizontal length scale of ~4 km. However, the r value reached 1.26 with the $b_x \sim -6.7 \times 10^{-7}$ s^{-2} and $H \sim 20$ m. As a result, destratification effect of the down-front wind exceeded restratification effect of the instabilities. Also note that Ri_b was even less than 0.25 near the front, indicating the existence of Kelvin-Helmholtz instability (Taylor & Ferrari, 2009).

3.3. High-Resolution Model Results

Off-coast bloom in late March of 2015 was also reproduced by the high-resolution nesting model to further demonstrate the contributions of submesoscale instabilities on driving off-coast near-surface stratification and bloom during NE wind relaxation. Horizontal resolution of ~0.6 km of the child grid is sufficient to resolve submesoscale processes in the TWS.

Figure 9 depicts the horizontal distributions of modeled sea-surface Chl-a, N^2, and nitrate concentration from 29 to 31 March in the TWS. With the NE wind existing on 29 March (Figure 5m), modeled Chl-a remained relatively low (roughly 2–3 mg m^{-3}) and distributed nearshore (Figure 9a). When the NE wind relaxed to zero and turned SW from 30 to 31 March (Figure 5m), the modeled Chl-a was increasing significantly (reaching 5 mg m^{-3}) and stretching off-coast, leading to an off-coast bloom (Figures 9b and 9c). Modeled sea-surface Chl-a (Figure 9c) reasonably reproduced the spatial pattern of the concurrent satellite Chl-a (Figure 2d) on 31 March, despite of the overall higher model values. Note that both model and satellite Chl-a presented signatures of submesoscale perturbations and eddies. During the bloom development, rapid restratification (Figures 9e and 9f) was occurring near the surface, corresponding to the off-coast extending of the along-shore front, as denoted by the isopycnal

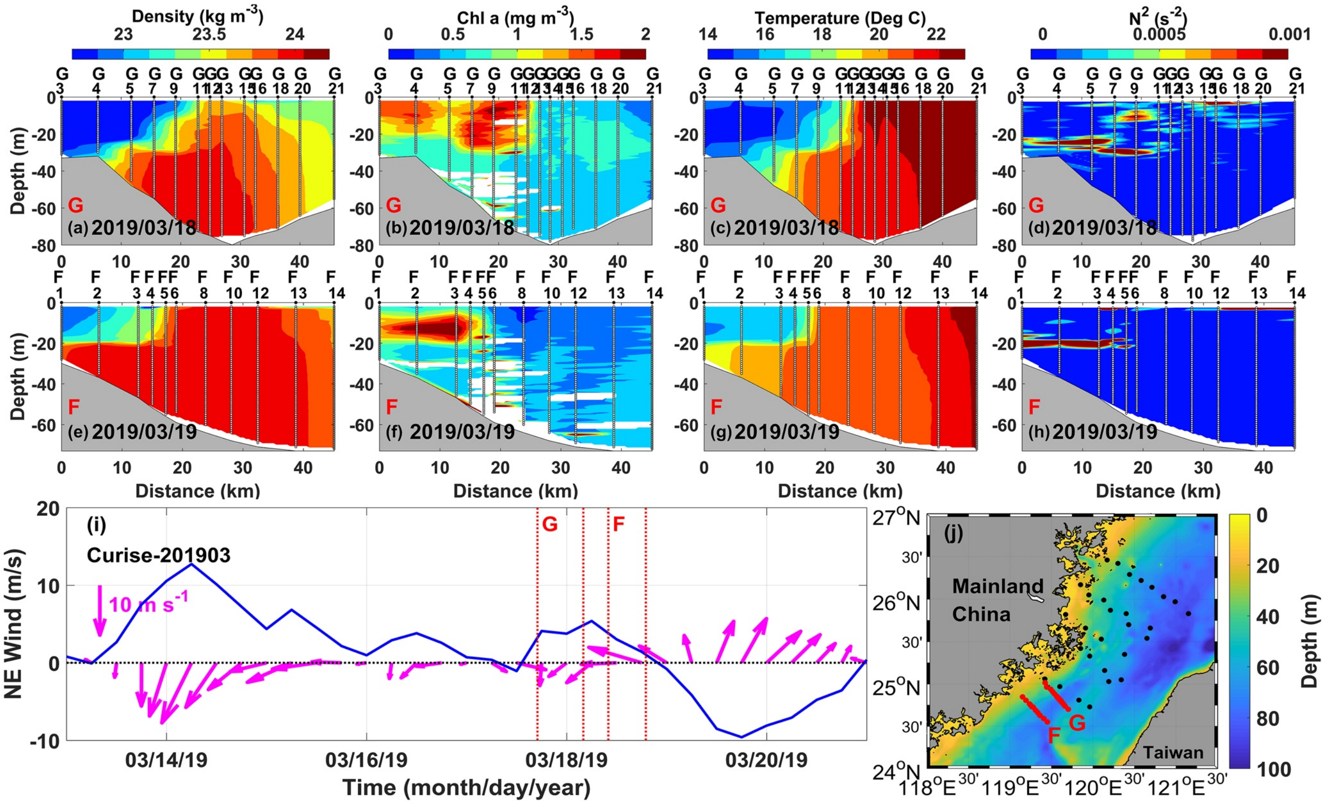

Figure 7. Cross-shore density (a, e), fluorometric Chl-a (b, f), temperature (c, g), and buoyancy frequency (d, h) at sections G and F (see map inset in j). Observation stations are labeled across the top, and white dots indicate the sample points for each station. (i) Time series of wind vectors (magenta arrows) and the along-shore component (blue line) over the stations (dashed blue box in Figure 1b) in middle March of 2019. Red dashed lines indicate cruise times for each section. Note the different color scale used for density and Chl-a to present the fine spatial structure, as compared with low-resolution cruises.

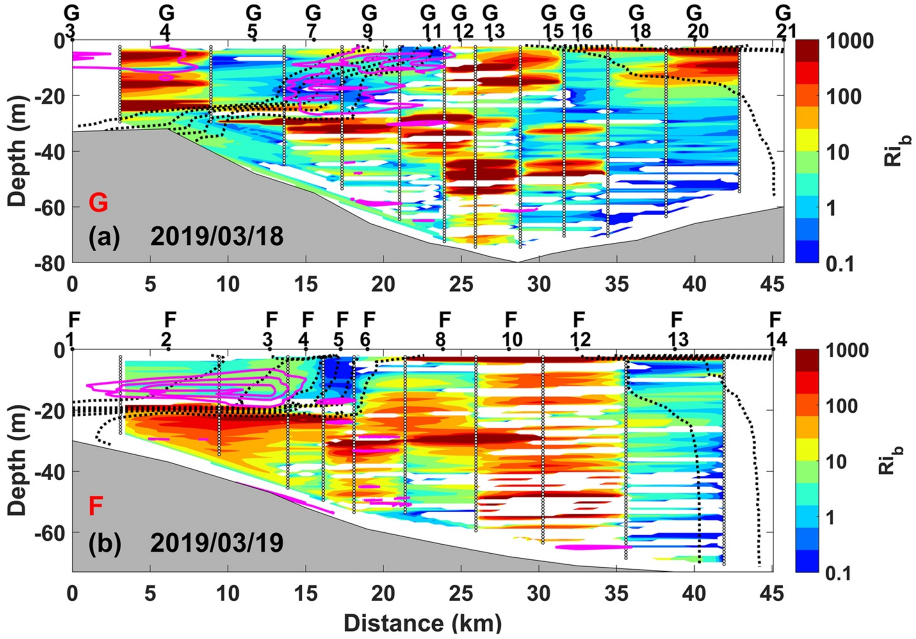

Figure 8. Cross-shore balanced Richardson number (Ri_b) at high-resolution sections G (a) and F (b). Observation stations are labeled across the top, and white dots indicate the calculation points. Magenta solid contours indicate observed Chl-a, with contour interval of 0.25 mg m^{-3}. Black dashed contours indicate observed density, with contour interval of 0.15 kg m^{-3}.

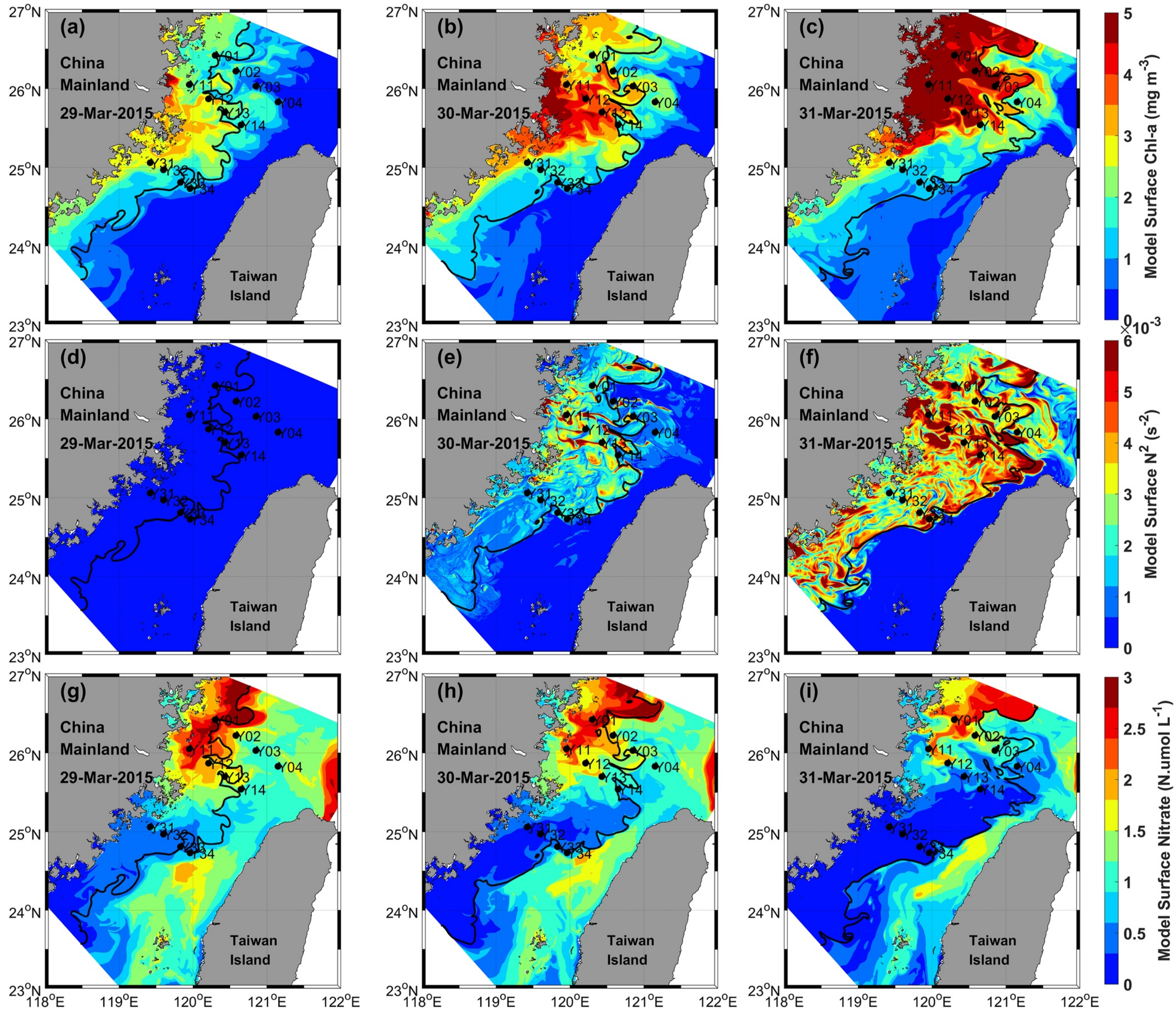

Figure 9. Modeled sea-surface Chl-a (a–c), N^2 (d–f), and nitrate concentration (g–i) from March 29 to 31, 2015. Black contours denote the isopycnal of 22 kg m^{-3}. Cruise stations in late March of 2015 are presented as black dots.

of 22 kg m^{-3}. In the meantime, sea-surface nitrate was being consumed rapidly by the growing phytoplankton (Figures 9h and 9i). Note that high Chl-a, N^2, and nitrate always distributed mainly on the nearshore side of the along-shore front during the blooming (e.g., Figures 9c, 9f and 9i).

On the other hand, Figure 10 shows the bloom development at section Y1 from 29 to 31 March. As described above, modeled Chl-a remained relatively low with tilted isopycnals on 29 March (Figure 10a). Afterward, Near-surface Chl-a (Figures 10e and 10i) was evidently increasing with the rapidly shallower isopycnals and increasing N^2 (Figures 10g and 10k) on 30 and 31 March, especially between the off-coast stations Y12 and Y14. On the other hand, the increasing off-coast phytoplankton rapidly consumed the available nitrate near the surface (Figures 10f and 10j). The high-resolution model robustly reproduced the cross-shore spatial structure of cruise-observations at section Y1 on 31 March. Observed and modeled Chl-a consistently show high Chl-a near the surface between stations Y12 and Y14, reaching ~20-m depth (Figures 5f and 10i). In the meantime, observed and modeled density exhibit intense near-surface restratification process (Figures 5h and 10k). In addition, observed and modeled nitrate present tendency of transport along-isopycnally from nearshore to off-coast surface, and nitrate near the station Y13 has been largely consumed by the growing phytoplankton there

(Figures 5g and 10j). On the whole, the high-resolution model is sufficiently robust to reproduce bloom development in the TWS, despite of the overall higher and lower values of the modeled Chl-a and nitrate relative to the observations, respectively.

The following diagnoses illustrate the significance of submesoscale instabilities on the off-coast restratification near the surface. When the down-front NE wind persisted on 29 March (Figure 5m), negative PV developed within the upper 20-m where intense submesoscale fronts existed with tilted isopycnals, especially between off-coast stations Y12 and Y14 (Figure 10d). It suggests the existence of vigorous SI. Near the same region, vigorous BCI co-existed with positive BC and PKC terms (Figures 11a and 11c), effectively transferring mean potential energy to eddy energy (EPE and EKE, Figures 11b and 11d). SI and BCI-induced eddy buoyancy advection was largely positive near the surface 20-m region, restratifying the surface layer (Figure 12a); However, the down-front NE wind destratified the water column, as suggested by the negative mean buoyancy advection in the upper 20-m layer (Figure 12b).

When the wind turned to SW in the following two days of 30 and 31 March, SI and BCI were becoming weaker with shallowing isopycnals (e.g., Figures 10h, 11e, and 11g). The positive eddy buoyancy advection suggested significant restratification effects of the instabilities, especially in the upper 10-m of the mixed layer (Figures 12c and 12e); while the mean buoyancy advection were largely negative near the surface 10-m (Figures 12d and 12f). It is worthy to note that the positive eddy buoyancy advection showed spatial consistency with high $\underline{N}^2$ near the surface (Figures 10g and 10k). Hence, the intense near-surface restratification co-occurring with blooming was mainly driven by submesoscale instabilities. Note also that the mean buoyancy advection (Figures 12b, 12d and 12f) restratified the water column near the middle layer of ~20 m (Figures 10c, 10g and 10k), which mainly related to the larger-scale processes of the geostrophic adjustment and Ekman transport (Wang et al., 2016; Zhao et al., 2020). Likewise, the middle layer stratification was also observed by the high-resolution cruise in March 2018 (Figures 7d and 7h).

Contributions of physical and biological effects (such as near-surface restratification) on the off-coast blooming can be depicted by diagnoses of the Chl-a budget equation (Equation 14). From the plane view in Figure 13, the evolution rate of the sea-surface Chl-a was relatively low on March 29, suggesting the blooming was not starting yet (Figure 13a). Advection term was relatively large and mostly positive with perturbation advection dominating, especially on the offshore side of the along-shore front (Figures 13d, 13g and 13j). It was primarily driven by

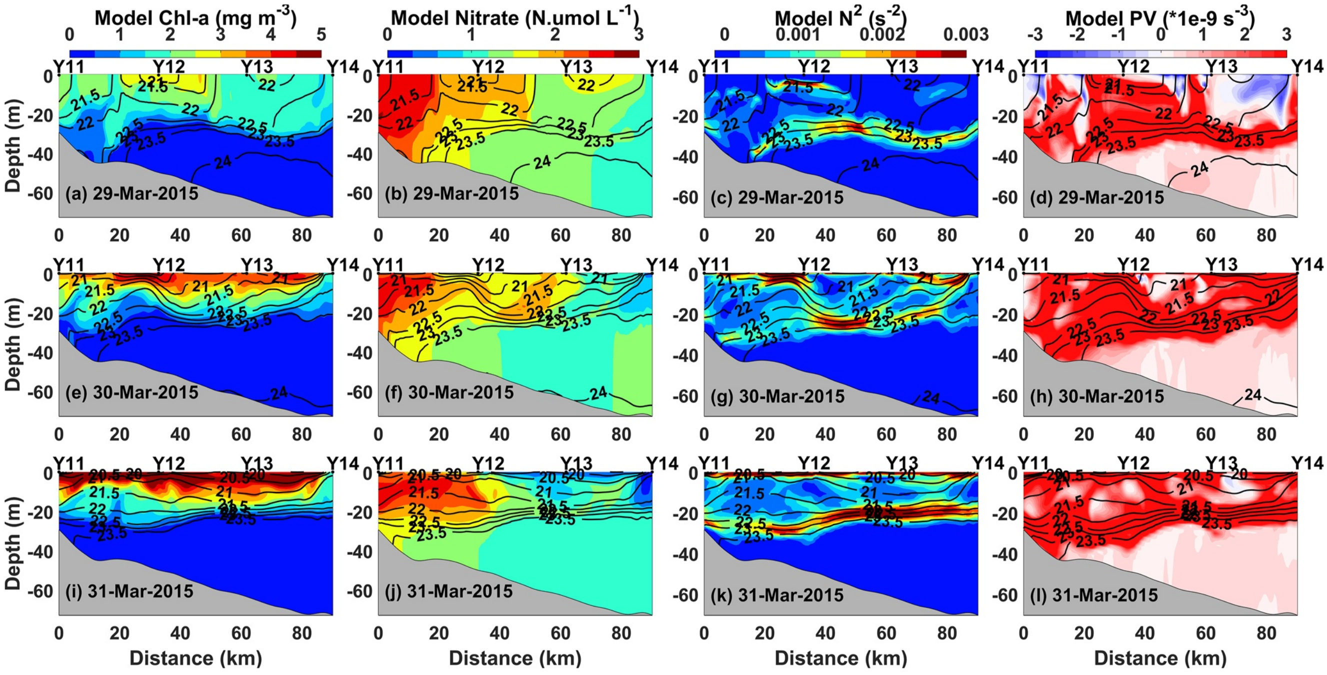

Figure 10. Modeled cross-shore Chl-a (a, e, i), nitrate concentration (b, f, j), N^2 (c, g, k), and Ertel PV (d, h, l) at section Y1 from 29 March to 31 March 2015. Black contours denote modeled isopycnals. Observation stations are labeled across the top.

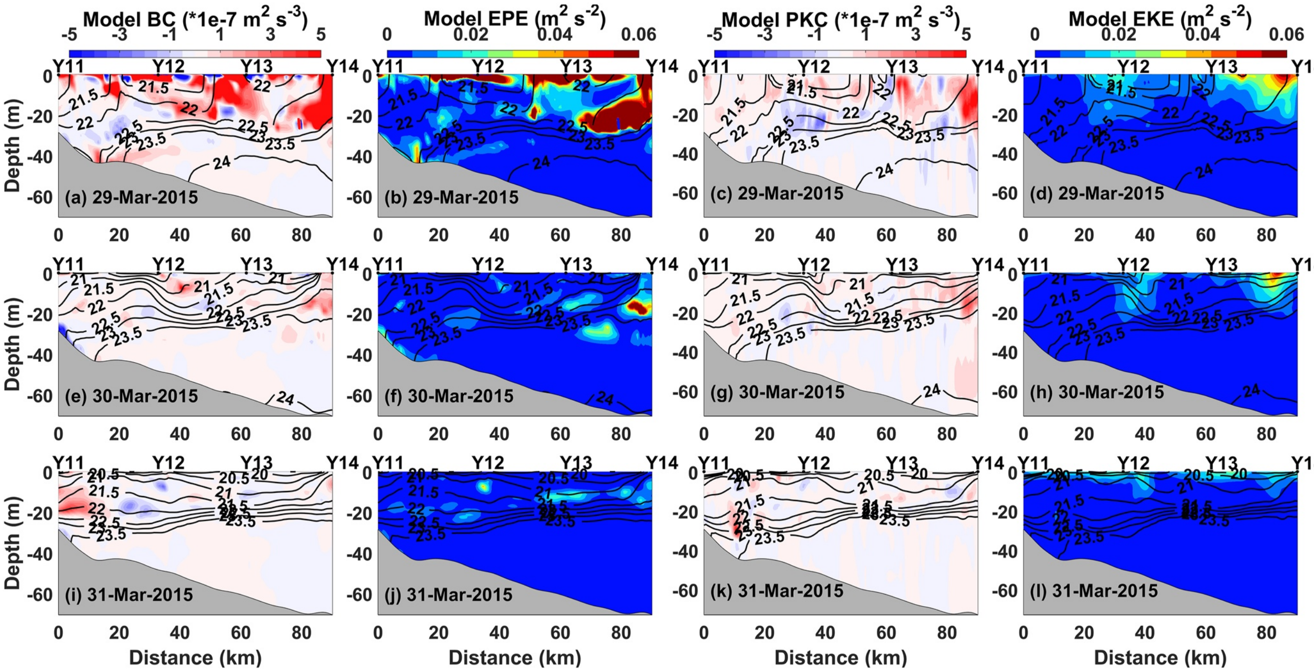

Figure 11. Modeled cross-shore BC term (a, e, i), EPE (b, f, j), PKC term (c, g, k), and EKE (d, h, l) at section Y1 from 29 March to 31 March 2015. Black contours denote modeled isopycnals. Observation stations are labeled across the top.

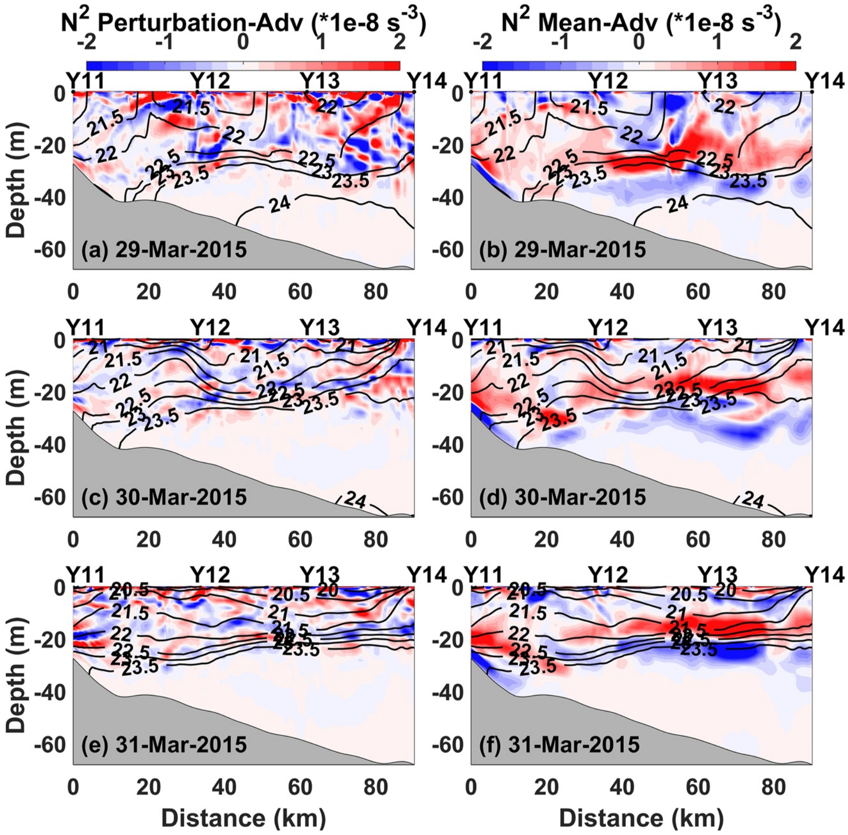

Figure 12. Modeled cross-shore eddy (a, c, e) and mean (b, d, f) buoyancy advection terms at section Y1 from 29 March to 31 March 2015. Black contours denote modeled isopycnals. Observation stations are labeled across the top.

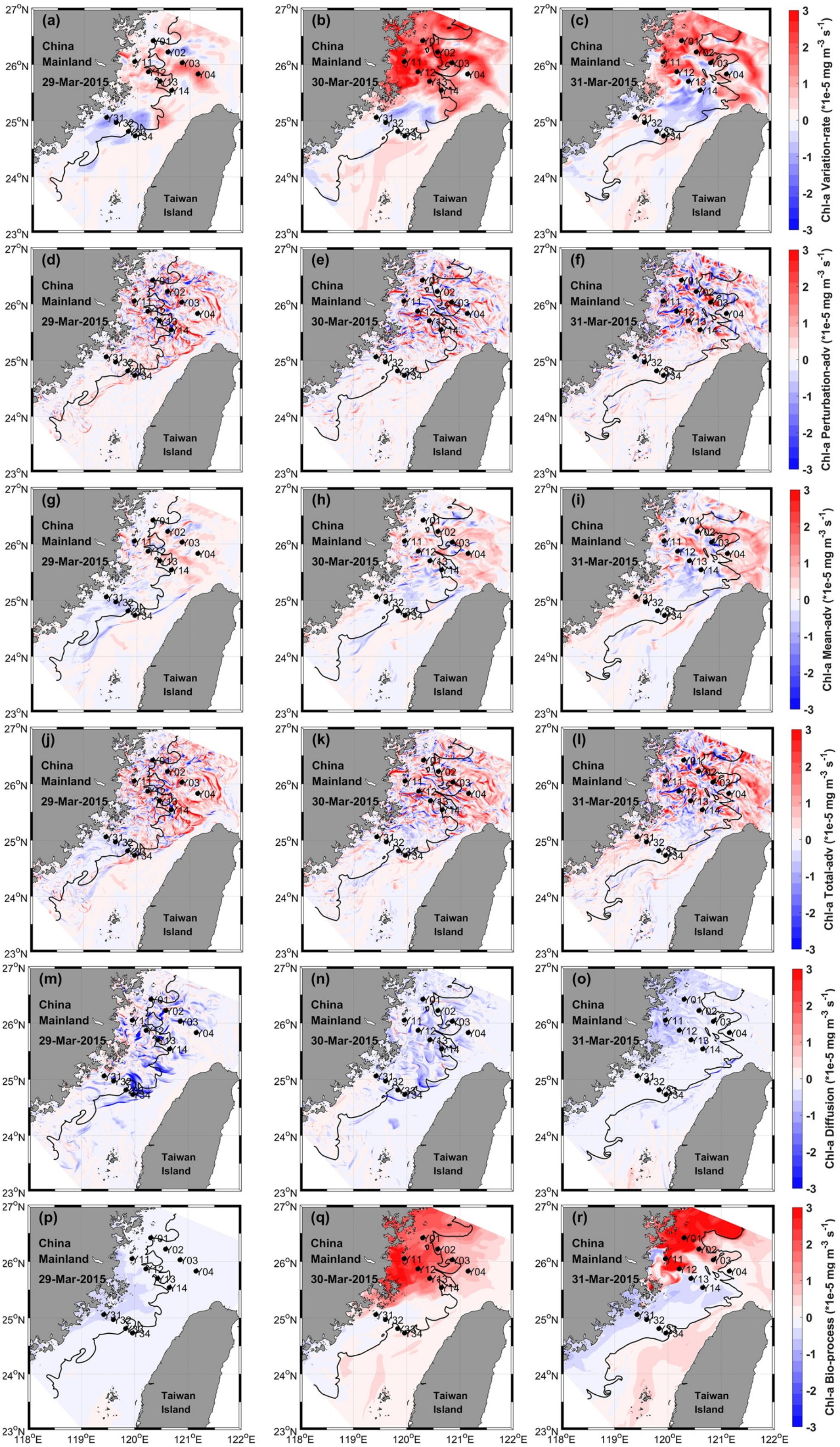

Figure 13. Modeled sea-surface Chl-a temporal variation rate (a–c), perturbation (d–f), mean (g–i), and total (j–l) advections, diffusion (m–o), and Bio term (p–r) in Chl-a budget equation from March 29 to 31, 2015. Black contours denote the isopycnal of 22 kg m^{-3}. Cruise stations in late March of 2015 are presented as black dots.

submesoscale instabilities and could transport nearshore Chl-a off the mainland coast. Diffusion term was also large while negative (Figure 13m) with weak surface stratification (Figure 9d) under NE wind (Figure 5m). The intense vertical mixing can inhibit phytoplankton growth, as concluded in previous studies (for example, Lewis et al., 1984; Taylor & Ferrari, 2011b). Consequently, the Bio term was relatively low and negative (Figure 13p) with weak phytoplankton growth (Figure S6a in Supporting Information S1), despite of the sufficient nitrate supply (Figure 9g). Beginning on March 30, the off-coast bloom was occurring, as presented by the positive and large Chl-a variation rate in Figure 13b. The increasing Chl-a was predominantly contributed by the positive Bio term (Figure 13q), where the process of phytoplankton growth was dominating (Figure S6b in Supporting Information S1). Diffusion term was weakened (Figure 13n) with near-surface restratification (Figure 9e). It trapped nutrients and phytoplankton cells within the euphotic layer, increasing light exposure and thus the phytoplankton growth rate (Mahadevan et al., 2012; Taylor & Ferrari, 2011a). The large Bio term distributed mainly on the nearshore side of the along-shore front (black contour in Figure 13q). Meanwhile, positive perturbation and mean advections distributed mainly on the offshore side of the front, suggesting the transport of growing Chl-a further offshore (Figures 13e, 13h and 13k). On 31 March, positive Chl-a evolution rate was moving northward with negative values covering the off-coast stations of section Y1 (Figure 13c). The increasing Chl-a northward of section Y1 was attributed to the positive Bio (Figure 13r) and advection terms (Figure 13l) distributed mainly on the nearshore and offshore sides of the along-shore front, respectively. The decreasing Chl-a southward of section Y1 was also related to the negative Bio (Figure 13r) and advection terms (Figure 13l) there. In terms of the biological processes, the positive Bio term northward of section Y1 was dominated by phytoplankton growth (Figure S6c in Supporting Information S1), which was closely related to surface stratification (Figure 9f) and nitrate availability (Figure 9i); while the negative Bio term southward of section Y1 was mainly due to phytoplankton mortality (Figure S6i in Supporting Information S1).

From the sectional view at section Y1 in Figure 14, the advection and Bio terms contributed to the blooming within different depth range. When the vertical diffusion term largely diminished on March 30 with the near-surface restratification process (Figures 14d and 14i), the Bio term increased significantly within the upper 10-m of the mixed layer (Figures 14e and 14j). It primarily contributed to the upper-layer Chl-a increment at section Y1 (Figure 14f). In the meantime, the perturbation advection term presented patchy structure and influenced the Chl-a evolution mainly within the upper 10-m layer (Figure 14g), related with submesoscale instabilities; while the contribution of the mean advection term was mostly positive and reached beyond the 20-m depth (Figure 14h), associated with larger-scale geostrophic adjustment and Ekman transport (Wang et al., 2016; Zhao et al., 2020). On 31 March, the Bio term decreased evidently (Figure 14o) due to the consumption of available nitrate near the surface, especially the off-coast region from station Y12 to Y14 (Figure 10j). With the contributions of the advection process (Figures 14l and 14m), the Chl-a evolution rate became largely negative near the

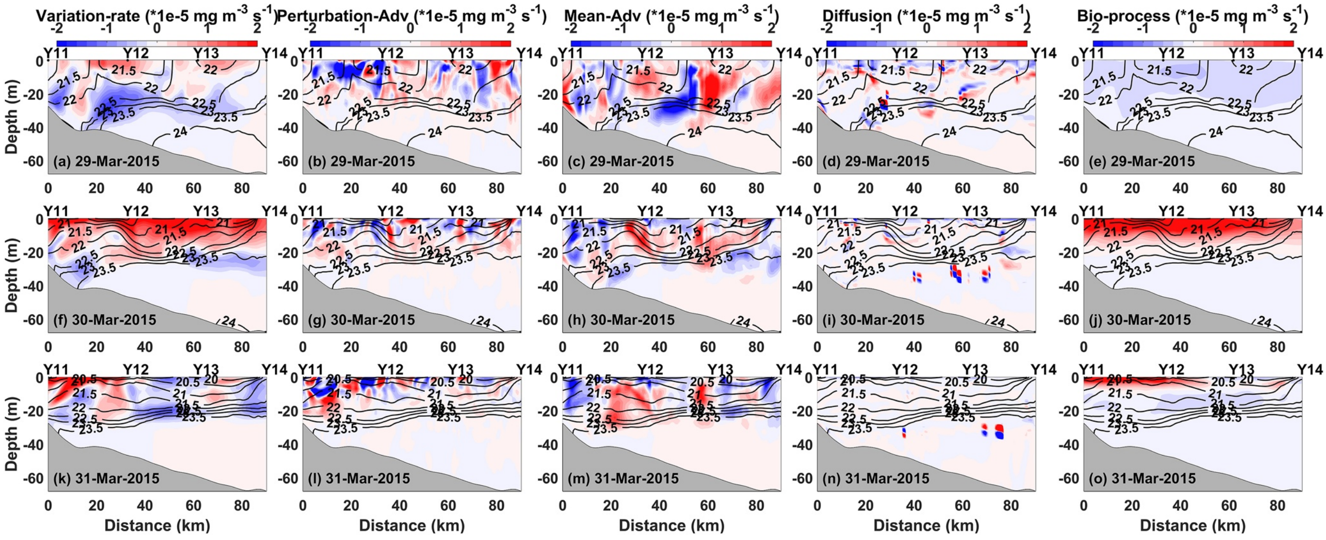

Figure 14. Modeled Chl-a temporal variation rate (a, f, k), perturbation (b, g, l) and mean (c, h, m) advections, diffusion (d, i, n), and Bio term (e, j, o) at section Y1 from 29 to 31 March 2015. Black contours denote modeled isopycnals. Observation stations are labeled across the top.

off-coast stations (Figure 14k). It suggested the off-coast bloom reached its maximum and began to disappear at section Y1.

Based on the high-resolution cruise observations and model results, the down-front NE wind could tilt the isopycnals and intensify the along-shore front, thus driving vigorous submesoscale SI and BCI in the TWS. When the NE wind relaxed, the submesoscale instabilities could induce rapid near-surface restratification and offshore stretching of the along-shore front within the upper 10-m mixed layer. It favored near-surface phytoplankton growth through the weakening of vertical diffusion, thus triggering bloom within a synoptic timescale of a few days. In the meantime, the surface 10-m phytoplankton could be entrained further offshore by the mean and eddy advection processes; while Chl-a increment reaching the middle 20-m was mainly contributed by the mean advection process during blooming.

As comparison, Wang et al. (2016) concluded that both the ∼20-m layer restratification and offshore advection due to larger-scale geostrophic adjustment triggered blooming during NE wind relaxation period. Nevertheless, this study emphasizes that near-surface restratification within the upper 10-m mixed layer was always a significant physical trigger for bloom development. Submesoscale instabilities could drive the rapid restratification and offshore stretching within the upper 10-m layer, favoring near-surface phytoplankton growth; while the contribution of larger-scale advection due to geostrophic adjustment and Ekman transport reached beyond ∼20-m depth.

3.4. Satellite Results

To further demonstrate the occurrence of TWS off-coast bloom during NE wind relaxation, a composite analysis of satellite sea-surface Chl-a and wind data from 1998 to 2018 was conducted. Figure S7 in Supporting Information S1 presents time series of the daily running-mean along-shore wind component for the 21 years (double-headed arrow in Figure 1b). The positive and negative values represent the NE and SW winds, respectively. A total of 48 NE wind relaxation events were observed, defined by 5 days of persistent NE wind followed by at least 2 days of SW wind, regardless of the wind magnitude, as denoted by the short red lines in Figure S7 in Supporting Information S1. These 48 events correspond well with the NE wind relaxation periods identified during the cruise investigation (e.g., the short red line in Figure 5m).

Figure 15 demonstrates the spatial distributions of the composite sea-surface Chl-a and temperature during different wind series scenarios. Meanwhile, the horizontal gradient of sea-surface temperature during NE wind relaxation is also presented to indicate the location of the along-shore front (contours in Figures 15c and 15f). In this sub-Section, we define the off-coast averaged Chl-a over 1.6 $mg \cdot m^{-3}$ as the criterion for the off-coast bloom (note that different bloom criterions are used due to the different Chl-a measurements by satellite and cruise). The off-coast area is defined by the sea-surface temperature gradient larger than 0.036°C m^{-1} during NE wind relaxation (blue contours in Figures 15c and 15f). Under the influence of strong NE wind, phytoplankton does not bloom with low off-coast Chl-a of roughly 1.21 $mg \cdot m^{-3}$ (Figure 15a), despite of the occupation of cold, light, and eutrophic CCC in the western strait (Figure 15d). Under the influence of strong SW wind, off-coast bloom does not develop either with low off-coast Chl-a of roughly 1.25 $mg \cdot m^{-3}$ (Figure 15b). The two scenarios testify that turbulent mixing by strong wind can inhibit off-coast phytoplankton growth (Lewis et al., 1984), and high Chl-a tends to distribute in the nearshore region (Figures 15a and 15b). In contrast, High off-coast averaged Chl-a exceeding 1.8 $mg \cdot m^{-3}$ presents during NE wind relaxation (Figure 15c), suggesting the occurrence of a phytoplankton bloom. Meanwhile, the location of the intense along-shore front (blue contours in Figures 15c and 15f, as the definition of the off-coast area) is highly consistent with the increment of off-coast Chl-a during bloom (Figures 15c and 15f). It further testifies NE wind relaxation is able to trigger off-coast bloom in the TWS, and the frontal processes are significant to the phytoplankton growth.

Time series of the along-shore winds and the off-coast surface Chl-a for the 7 composite days are demonstrated in Figure 16. Steady NE wind of approximately 7–8 $m \cdot s^{-1}$ persists for the first 4 days (red solid line in Figure 16a) and then relaxes to zero during the fifth day (the relaxation period). Subsequently, weak SW wind of around 1–2 $m \cdot s^{-1}$ develops for the last 2 days. According to the temporal evolution of off-coast Chl-a (green line in Figure 16b), the 7 days can be divided into three stages. During stage 1 (days −5 to −1), the off-coast Chl-a decreases and remains low (less than 1.4 $mg \cdot m^{-3}$) under the influence of NE wind. During stage 2 (days −1 to 0), the NE wind drops to zero and then turns into a weak SW wind. An incremental increase in off-coast Chl-a to nearly 1.82 $mg \cdot m^{-3}$ corresponds to the relaxing NE wind, supporting the conclusion that NE wind relaxation can trigger off-coast phytoplankton bloom within a synoptic timescale. During stage 3 (days 0–1), the bloom

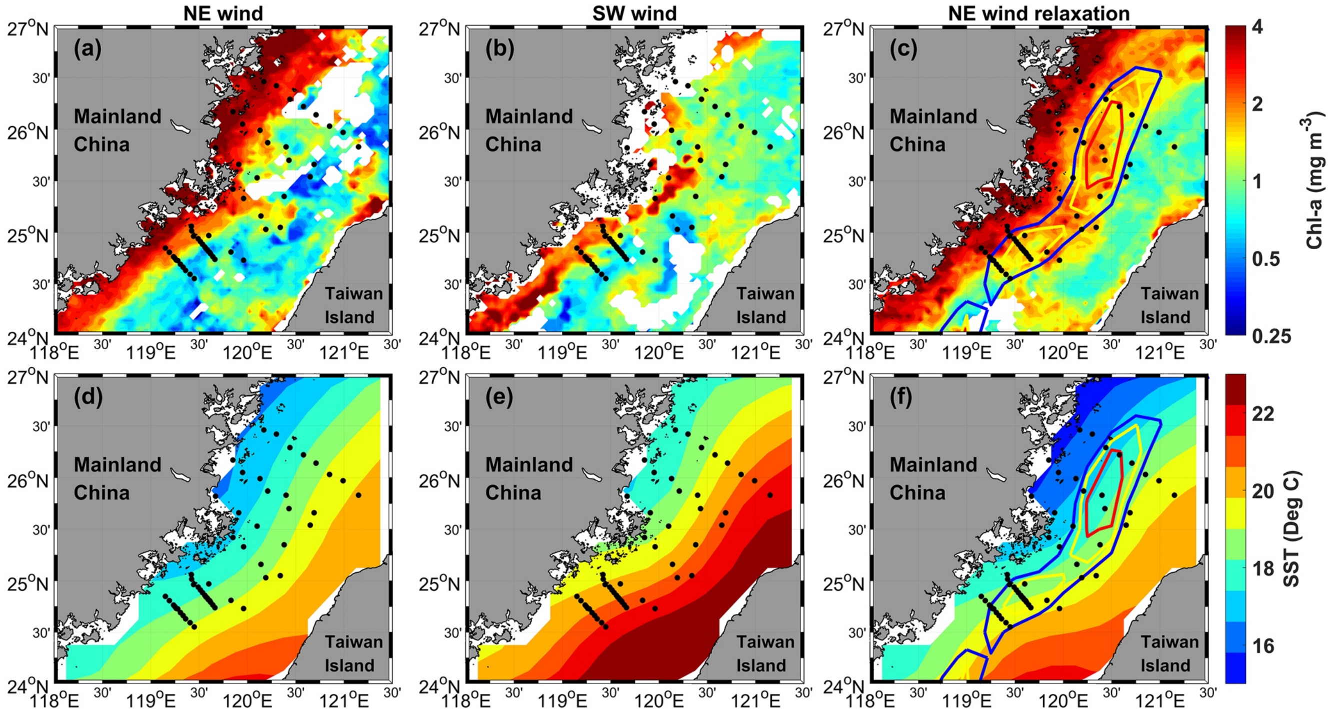

Figure 15. Single-day composite of sea-surface Chl-a in the northern TWS after 2-day consecutive NE winds stronger than 10.5 m s^{-1} (a), after 2-day consecutive SW winds stronger than 4.5 m s^{-1} (b), and during the NE wind relaxation periods (c). The corresponding composite maps of sea-surface temperature (shading) and its horizontal gradient during NE wind relaxation (contours, units: °C m^{-1}) (d, e, f). The red, yellow, and blue contours denote the values of the horizontal gradient of 0.04, 0.038, and 0.036, respectively. The blue contour in (c and f) indicates the off-coast area for calculating the off-coast Chl-a. The black dots denote cruise stations as in Figure 1b.

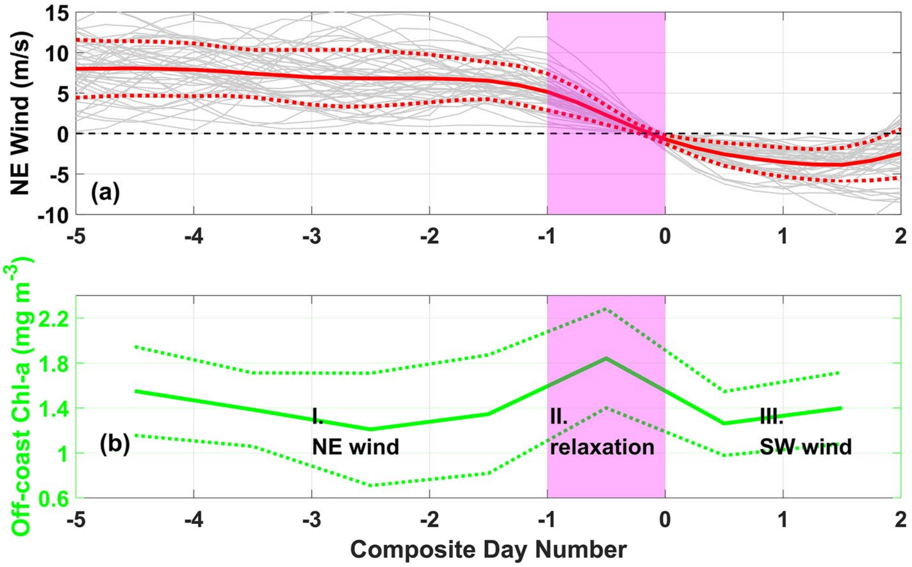

Figure 16. (a) All NE wind relaxation events identified in Figure S7 in Supporting Information S1 (gray lines), plotted 5 days before and 2 days after the wind changes direction. The composite mean is indicated by the red solid line and ±1 s.d. by the red dashed lines. (b) Composite sea-surface Chl-a averaged over the off-coast area (blue contour in Figure 15c) from day −5 to +2 of all the relaxation events. The green dashed lines indicate ±1 s.d. of the off-coast sea-surface Chl-a for each composite day. The wind relaxation and off-coast bloom period is from day −1 to 0, indicated by magenta shading.

disappears, and Chl-a drops back to roughly 1.3 mg·m^{-3} under the influence of the SW wind. Note that this composite analysis has statistical error due to severe intermittent cloud cover over the TWS. Variations in front intensity, riverine discharge, and nutrient supply in the TWS can also introduce uncertainties in this analysis.

Figure 17 presents the spatial pattern of phytoplankton growth during off-coast blooms. Bloom development corresponds to significant off-coast Chl-a increase during NE wind relaxation (Figure 17c). The maximum Chl-a increase in the off-coast region can exceed 1.0 mg·m^{-3}, with the averaged value of approximately 0.6 mg·m^{-3}. The off-coast Chl-a increment during bloom is spatially consistent with the along-shore front, extending nearly 50–100 km off the mainland coast. Cruise observations during NE wind relaxation consistently indicated that intense surface stratification (e.g., Figures 5d and 6h) and high Chl-a (e.g., Figures 5b and 6f) spread over a comparable distance off the mainland coast during off-coast blooming. Additionally, nitrate can be transported over the comparable distance from nearshore to offshore surface layer (e.g., Figures 5c and 6g), favoring off-coast phytoplankton growth. Note that satellite surface Chl-a data are more reliable off-coast than the nearshore data in the TWS.

SOM analysis was conducted using the 21-year remote sensing surface Chl-a data to extract three characteristic patterns in the TWS (Figure 18). The corresponding 7-day time series of the dominant winds (Figures 18d–18f) are also presented. Note that due to the vastly different data types and temporal coverage, the three SOM categories do not directly correspond to those of the cruise data. The three types are roughly consistent with the three categories in terms of the dominant wind temporal variation, however.

Type I demonstrates that Chl-a is lower off-coast (averaged value of 1.58 mg·m^{-3}, Figure 18a) under moderate NE wind (roughly 5 m·s^{-1}, Figure 18d). Type II shows significantly high surface Chl-a (averaged value of 2.34 mg·m^{-3}, Figure 18b) spreading near 50–100 km off-coast during NE wind relaxation (Figure 18e). Type III demonstrates that Chl-a is lowest near the off-coast region (averaged value of 1.31 mg·m^{-3}, Figure 18c) under SW wind (Figure 18f). The off-coast bloom development during NE wind relaxation can be clearly seen from the Chl-a increment in Figures 18g and 18h. SOM analysis reveals that relatively low off-coast Chl-a frequently occurs under NE or SW wind (48.8% and 34.1% of all occurrences, respectively), whereas off-coast blooms during NE wind relaxation account for only 17.1%. The occurrence frequencies derived from the SOM

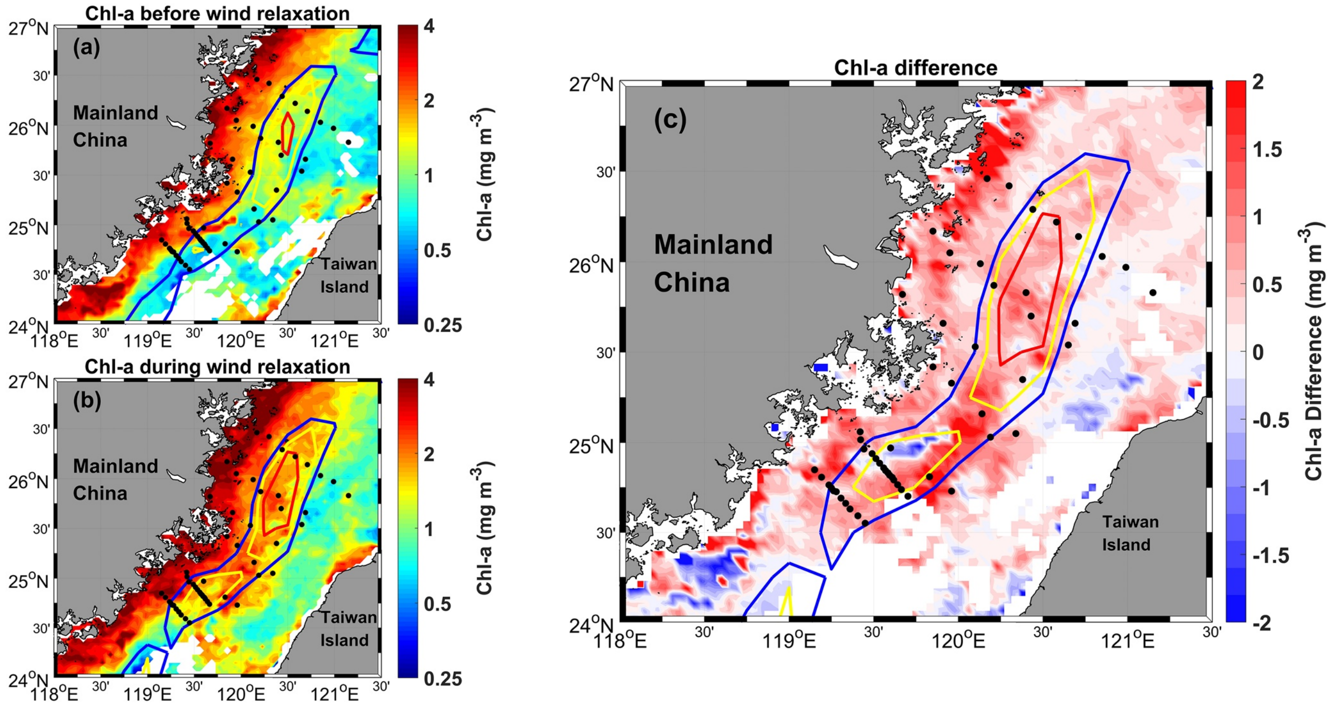

Figure 17. The composite of sea-surface Chl-a for (a) day −2 to −1 and (b) day −1 to 0 of the wind relaxation events of Figure 16 and (c) their difference (b minus a). The red, yellow, and blue contours denote the values of the corresponding sea-surface temperature horizontal gradient of 0.040, 0.038, and 0.036, respectively (units: °C m^{-1}). Cruise stations (Figure 1b) are indicated by black dots. The blue contour in (b and c) indicates the off-coast area for calculating the off-coast Chl-a.

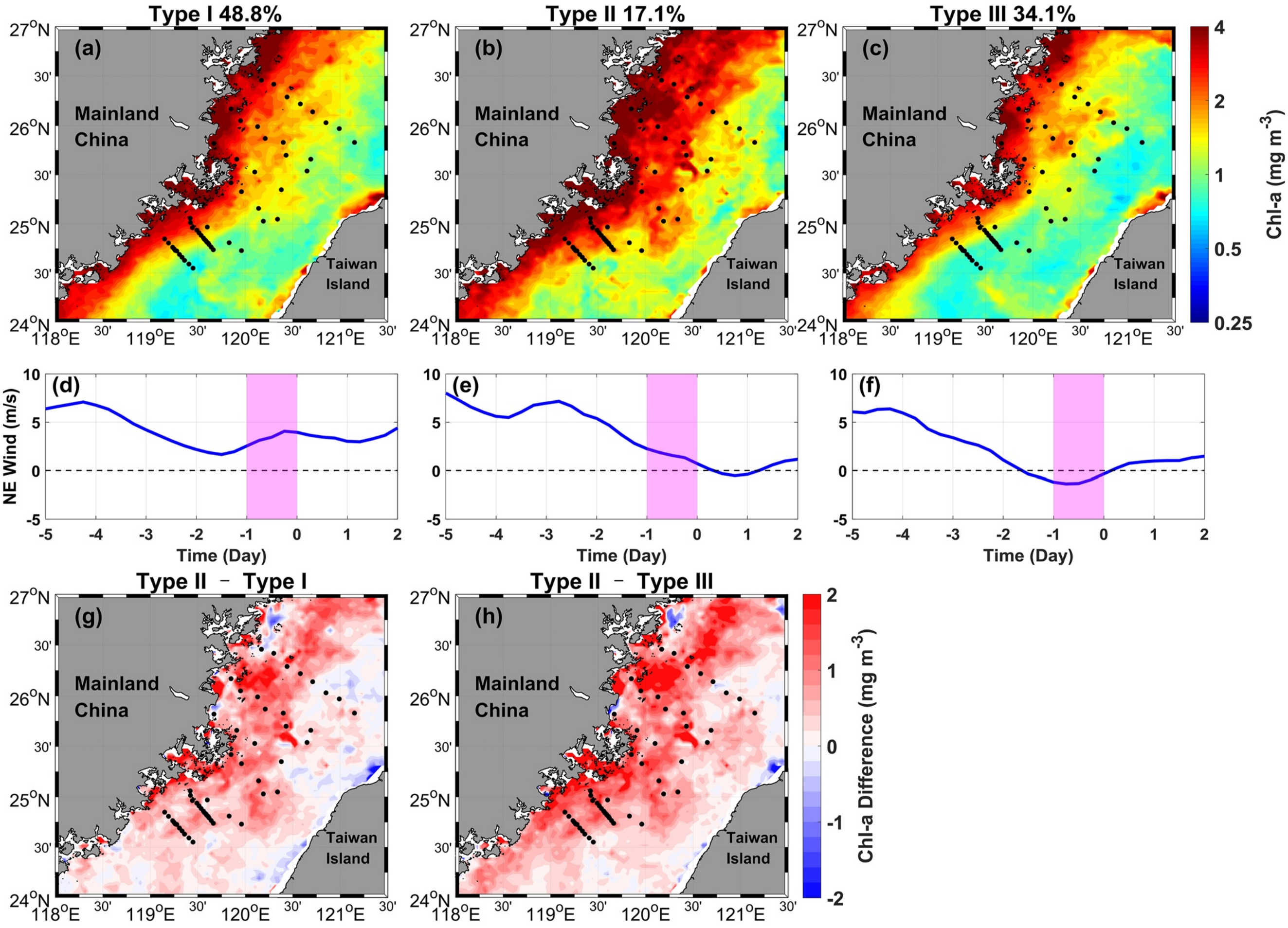

Figure 18. A three-by-one self-organizing map (SOM) of sea-surface Chl-a (a–c) and the corresponding wind time series (d–f). The frequency of occurrence (in percentage) is listed on the upper panels. Magenta shading denotes the period of remote sensing Chl-a. Sea-surface Chl-a difference (g) between Type II and Type I (b minus a), as well as difference (h) between Type II and Type III (b minus c).

of satellite data differ from those derived from cruise data as the cruise data are heavily biased toward the NE wind relaxation.

Although satellite Chl-a is overall higher than the cruise observation due to the satellite inversion algorithm, the significant off-coast Chl-a increment during the NE wind relaxation period is consistent in both data sets. In a short summary, composite analysis of the 21-year sea-surface Chl-a and wind data further confirm that NE wind relaxation can trigger off-coast bloom in the TWS. The bloom can develop within a synoptic timescale (Figure 16), and has a significant spatial consistency with the along-shore front (Figure 17). The results further suggest that frontal instabilities play a significant role in the off-coast blooming.

4. Discussion

4.1. Different Contributions of SI and BCI on Blooming

High-resolution cruise observations and model results consistently testify the existence of SI near the along-shore front region during the off-coast blooming in the TWS. As noted by the previous researches, SI is able to drive vigorous along-isopycnal exchange of tracers within the water column (Bachman et al., 2017; Bachman & Taylor, 2014). Likewise, cruise and model data show that nearshore nitrate tended to be transported toward the offshore euphotic layer along the isopycnals, especially near the pycnocline, during both the NE wind (Figure 3) and NE wind relaxation periods (Figures 5 and 10). Therefore, it is reasonable to speculate that this nutrient transport could be significantly attributed to SI, which was conducive to the off-coast phytoplankton growth during near-surface restratification. In contrast, nitrate located comparably nearshore relative to the fresher water under the up-front SW wind (Figure 4), indicating that nearshore nitrate could not be transported offshore effectively without SI. This topics is worthy to be explored using the model results.

Moreover, previous studies have reported that SI is a two-dimensional process independent of the along-front direction, whereas BCI is three-dimensional with meanders and eddies developing along fronts (Taylor & Ferrari, 2011a). Therefore, different roles SI and BCI play in triggering off-coast bloom can be explored using idealized model experiments.

4.2. Chl-a Spatial Variability During Bloom

Along-shore Chl-a heterogeneity was also revealed by the cruise during off-coast bloom (e.g., Figure 5). It can be explained by several factors, for example, cruise time; spatiotemporal evolution of the dominant wind (Brink & Seo, 2016) and the along-shore front; spatial variation of coastline and topography (Durski & Allen, 2005); riverine discharge and nutrient supply (Hong, Chai, et al., 2011); current advection, etc. For example, observation at section Y3 presented weaker stratification (Figure 5l) and lower Chl-a (Figure 5j) compared with sections Y1 and Y2, presumably because cruise at section Y3 was conducted earlier, so that surface stratification and blooming had not fully developed. In addition, previous studies also reported that various continental slopes correspond to different levels of BCI development. The flatter the continental slope is, more intense the instability will develop (Brink, 2012; Brink & Cherian, 2013). Therefore, steeper slope at section Y3 might result in weaker instability-induced restratification and bloom.

4.3. Biological Effects and Significances

Phytoplankton is responsible for roughly half of the global primary production (Longhurst et al., 1995). It usually does not grow uniformly but is rather punctuated by patchy blooms lasting for several days (Dutkiewicz et al., 2001), consistent with submesoscale processes (Mahadevan, 2016). Oceanic phytoplankton blooms play a significant role in increasing primary production and significantly contributes to global photosynthetic carbon fixation (Lu, Luo, et al., 2018; Sabine et al., 2004). Therefore, the spatiotemporal heterogeneity of phytoplankton should be better understood to improve estimates of global primary production and ocean carbon uptake.

Oceanic phytoplankton blooms are impacted not only by multi-scale physical processes (for example, Lu, Oey, et al., 2018; Lu et al., 2017; Wang et al., 2021), but also by biological processes. The high-resolution model results show that phytoplankton mortality was mainly responsible for the decrement of Chl-a during bloom, compared with other processes such as zooplankton grazing (Figure S6 in Supporting Information S1). However, Calbet and Landry (2004) reported that microzooplankton consumption is the main source of phytoplankton mortality in the oceans. The ratio of phytoplankton growth and microzooplankton grazing varies modestly among various oceanic regions, ranging from 60% for coastal regions to 70% for the open oceans. In addition, Strom et al. (2001) found that microzooplankton grazing accounts for 78% and 42% of the phytoplankton growth during phytoplankton blooms and low biomass periods, respectively, in two productive coastal regions of the North Pacific. Consistently, in situ measurements in the summer TWS also presented significant grazing pressure of the microzooplankton on the primary productivity, reaching 71% ~ 281% in Zeng et al. (2006) and 40% ~ 151% in Zeng and Huang (2012). It indicates that microzooplankton grazing is one of the primary reasons for the phytoplankton mortality in the TWS, especially during the off-coast bloom. Similar story was also found in the adjacent ECS (Sun et al., 2003) and northern SCS (Zheng et al., 2012). Consequently, the disappearance the off-coast bloom roughly 1–2 days after the NE wind relaxation (Figure 16) is possibly due to the increased microzooplankton consumption. Certainly, this biological process needs to be further testified. Note also missing values of the remote sensing Chl-a may also influence the composite temporal variation of Chl-a.

Off-coast blooms in the TWS also have other ecological and biological significances. For example, they may influence the biogeochemical characteristics of the adjacent waters, such as the ECS and SCS, considering the complicated current system (Hu et al., 2010). In the meantime, the domination of different species in different bloom scenarios (Hong, Chai, et al., 2011) may also have ecological impacts.

Therefore, further interdisciplinary studies are required to more comprehensively understand the mechanism and concomitant biological and ecological consequences of the off-coast phytoplankton bloom observed in this study.

Table 1
Summary of Contributions of the Instability-Related Processes on the Off-Coast Blooming for the Low-Resolution Cruises in the TWS

Cruise	Dominant wind	Restratification by submeso processes SI and/or BCI	Nutrient supply by SI	Bloom
2012,02	NE wind	No	Yes	No
2014,04	SW wind	No	No	No
2015,03				
2015,11	NE wind Relaxation	Yes	Yes	Yes
2016,03				
2018,03				

5. Summary and Conclusion

Phytoplankton growth and Chl-a concentration during different wind series scenarios were comprehensively analyzed using multi-year cruise, model and satellite data in the TWS. Through composite and SOM analyses, the three data sets consistently show that strong NE and SW winds could inhibit phytoplankton growth, whereas NE wind relaxation favored off-coast phytoplankton growth and triggered blooming near the surface. The off-coast bloom developed within a few days and spread near 50–100 km off the mainland coast, co-locating with the along-shore front in the TWS.

High-resolution cruise observations and model results were applied to demonstrate the intrinsic mechanisms of the off-coast bloom. As shown by both data sets, the down-front NE wind could tilt the isopycnals and intensify the along-shore front, thus driving the development of submesoscale SI and BCI near the along-shore front in the TWS. Subsequently when the NE wind was relaxing, the vigorous submesoscale instabilities could induce rapid near-surface restratification and offshore stretching of the along-shore front near the surface 10-m of the mixed layer within a synoptic timescale of a few days. The intense surface stratification trapped phytoplankton cells and available nutrients within the surface euphotic layer, increasing light exposure and favoring phytoplankton growth off the mainland coast. In the meantime, the surface 10-m phytoplankton could be entrained further offshore by the mean and eddy advection processes; while Chl-a increment reaching the 20-m depth was mainly contributed by the mean advection process, which was associated with larger-scale geostrophic adjustment and Ekman transport. Furthermore, cruise and model data exhibit tendency of nitrate transport from nearshore toward the offshore euphotic layer along isopycnals during off-coast blooming. This process was conducive to the off-coast phytoplankton growth and is reasonably speculated to be driven by the along-isopycnal mixing effects of SI.

Contributions of the instability-related processes on the off-coast blooming for the low-resolution cruises can be summarized in Table 1. The processes include near-surface restratification and offshore nutrient supply. For NE wind series, the latter condition was satisfied but not the former. For SW wind series, neither of the two conditions were met. Both conditions were available for NE wind relaxation series. Therefore, off-coast phytoplankton bloom only developed during NE wind relaxation. In all, this study shows that submesoscale instabilities of SI and BCI near the along-shore front play a significant role in triggering the off-coast bloom during the down-front NE wind relaxation in the TWS.

Conflict of Interest

The authors have no conflicts of interest to declare. All co-authors have seen and agree with the contents of the manuscript and there is no financial interest to report. We certify that the submission is original work and is not under review at any other publication.

Data Availability Statement

The in situ cruise data in the TWS analyzed in Section 3 of this study are from the Shared Cruise Program, Natural Science Foundation of China (NSFC), which are available openly at Science Data Bank with https://doi.org/10.57760/sciencedb.02330 and can also be applied online at https://www.sss-nsfc.org.cn/home. The daily sea-surface Chl-a remote sensing data used for composite and SOM analysis in Section 4 of this study are from the Ocean Color Climate Change Initiative (OC-CCI) data set, Version 4.0, European Space Agency, available online at https://esa-oceancolour-cci.org. The sea-surface wind data used for composite and SOM analysis in Section 4 of this study are from the National Centers for Environmental Predictions (NCEP)-DOE Reanalysis 2 data set (Kanamitsu et al., 2002), available online at http://www.cpc.ncep.noaa.gov/products/wesley/reanalysis2. The sea-surface temperature data used in Section 4 of this study are from the Optimum Interpolation sea-surface temperature (OISST, Huang et al., 2021) data set, Version 2.1, NOAA Physical Sciences Laboratory (PSL), available online at https://psl.noaa.gov/data/gridded/data.noaa.oisst.v2.highres.html.

Acknowledgments
This work was supported by grant (U1805241, 41876004) from Natural Science Foundation of China (NSFC). S. Fang, Y. Yu and Z. Xu from Information and Network Center of Xiamen University are acknowledged for the help with the high-performance computing.

References

Bachman, S. D., Fox-Kemper, B., Taylor, J. R., & Thomas, L. N. (2017). Parameterization of frontal symmetric instabilities. I: Theory for resolved fronts. *Ocean Modelling*, *109*, 72–95. https://doi.org/10.1016/j.ocemod.2016.12.003

Bachman, S. D., & Taylor, J. R. (2014). Modelling of partially-resolved oceanic symmetric instability. *Ocean Modelling*, *82*, 15–27. https://doi.org/10.1016/j.ocemod.2014.07.006

Bianchi, T. S., Lambert, C., & Biggs, D. C. (1995). Distribution of chlorophyll-a and pheopigments in the northwestern gulf-of-Mexico—Ā comparison between fluorometric and high-performance liquid-chromatography measurements. *Bulletin of Marine Science*, *56*(1), 25–32.

Bidigare, R. R., Kennicutt, M. C., & Brooks, J. M. (1985). Rapid-determination of chlorophylls and their degradation products by high-performance liquid-chromatography. *Limnology & Oceanography*, *30*(2), 432–435. https://doi.org/10.4319/lo.1985.30.2.0432

Boccaletti, G., Ferrari, R., & Fox-Kemper, B. (2007). Mixed layer instabilities and restratification. *Journal of Physical Oceanography*, *37*(9), 2228–2250. https://doi.org/10.1175/jpo3101.1

Brannigan, L. (2016). Intense submesoscale upwelling in anticyclonic eddies. *Geophysical Research Letters*, *43*(7), 3360–3369. https://doi.org/10.1002/2016gl067926

Brink, K. H. (2012). Baroclinic instability of an idealized tidal mixing front. *Journal of Marine Research*, *70*(4), 661–688. https://doi.org/10.1357/002224012805262716

Brink, K. H., & Cherian, D. A. (2013). Instability of an idealized tidal mixing front: Symmetric instabilities and frictional effects. *Journal of Marine Research*, *71*(6), 425–450. https://doi.org/10.1357/002224013812587582

Brink, K. H., & Seo, H. (2016). Continental shelf baroclinic instability. Part II: Oscillating wind forcing. *Journal of Physical Oceanography*, *46*(2), 569–582. https://doi.org/10.1175/jpo-d-15-0048.1

Calbet, A., & Landry, M. R. (2004). Phytoplankton growth, microzooplankton grazing, and carbon cycling in marine systems. *Limnology & Oceanography*, *49*(1), 51–57. https://doi.org/10.4319/lo.2004.49.1.0051

Capet, X., McWilliams, J. C., Mokemaker, M. J., & Shchepetkin, A. F. (2008). Mesoscale to submesoscale transition in the California current system. Part I: Flow structure, eddy flux, and observational tests. *Journal of Physical Oceanography*, *38*(1), 29–43. https://doi.org/10.1175/2007jpo3671.1

Chang, Y. L., & Oey, L. Y. (2011). Frontal circulation induced by up-front and coastal downwelling winds. *Ocean Dynamics*, *61*(9), 1345–1368. https://doi.org/10.1007/s10236-011-0435-2

Chapman, D. C. (1985). Numerical treatment of cross-shelf open boundaries in a barotropic coastal ocean model. *Journal of Physical Oceanography*, *15*(8), 1060–1075. https://doi.org/10.1175/1520-0485(1985)015<1060:Ntocso>2.0.Co;2

Chen, C. C., Shiah, F. K., Chung, S. W., & Liu, K. K. (2006). Winter phytoplankton blooms in the shallow mixed layer of the South China Sea enhanced by upwelling. *Journal of Marine Systems*, *59*(1–2), 97–110. https://doi.org/10.1016/j.jmarsys.2005.09.002

Chen, Z. Y., Yan, X. H., & Jiang, Y. W. (2014). Coastal cape and canyon effects on wind-driven upwelling in northern Taiwan Strait. *Journal of Geophysical Research-Oceans*, *119*(7), 4605–4625. https://doi.org/10.1002/2014jc009831

Dafner, E. V. (2015). Segmented continuous-flow analyses of nutrient in seawater: Intralaboratory comparison of Technicon AutoAnalyzer II and Bran+Luebbe continuous flow AutoAnalyzer III. *Limnology and Oceanography: Methods*, *13*(10), 511–520. https://doi.org/10.1002/lom3.10035

Durski, S. M., & Allen, J. S. (2005). Finite-amplitude evolution of instabilities associated with the coastal upwelling front. *Journal of Physical Oceanography*, *35*(9), 1606–1628. https://doi.org/10.1175/jpo2762.1

Dutkiewicz, S., Follows, M., Marshall, J., & Gregg, W. W. (2001). Interannual variability of phytoplankton abundances in the North Atlantic. *Deep-Sea Research Part II*, *48*(10), 2323–2344. https://doi.org/10.1016/s0967-0645(00)00178-8

Egbert, G. D., & Erofeeva, S. Y. (2002). Efficient inverse Modeling of barotropic ocean tides. *Journal of Atmospheric and Oceanic Technology*, *19*(2), 183–204. https://doi.org/10.1175/1520-0426(2002)019<0183:Eimobo>2.0.Co;2

Fennel, K., Wilkin, J., Levin, J., Moisan, J., O'Reilly, J., & Haidvogel, D. (2006). Nitrogen cycling in the Middle Atlantic Bight: Results from a three-dimensional model and implications for the North Atlantic nitrogen budget. *Global Biogeochemical Cycles*, *20*(3), 14. https://doi.org/10.1029/2005gb002456

Flather, R. A. (1976). A tidal model of northwest European continental shelf. *Mémoires de la Société royale des sciences de Liège*, *6*(10), 141–164.

Fox-Kemper, B., Ferrari, R., & Hallberg, R. (2008). Parameterization of mixed layer eddies. Part I: Theory and diagnosis. *Journal of Physical Oceanography*, *38*(6), 1145–1165. https://doi.org/10.1175/2007jpo3792.1

Freilich, M., & Mahadevan, A. (2021). Coherent pathways for subduction from the surface mixed layer at ocean fronts. *Journal of Geophysical Research-Oceans*, *126*(5), 18. https://doi.org/10.1029/2020jc017042

Geider, R. J., MacIntyre, H. L., & Kana, T. M. (1996). A dynamic model of photoadaptation in phytoplankton. *Limnology & Oceanography*, *41*(1), 1–15. https://doi.org/10.4319/lo.1996.41.1.0001

Geider, R. J., MacIntyre, H. L., & Kana, T. M. (1997). Dynamic model of phytoplankton growth and acclimation: Responses of the balanced growth rate and the chlorophyll a: Carbon ratio to light, nutrient-limitation and temperature. *Marine Ecology Progress Series*, *148*(1–3), 187–200. https://doi.org/10.3354/meps148187

Gu, C., Li, H., Xu, F. H., Cheng, P., Wang, X. H., Xu, S. M., & Peng, Y. R. (2018). Numerical study of Jiulongjiang river plume in the wet season 2015. *Regional Studies in Marine Science*, *24*, 82–96. https://doi.org/10.1016/j.rsma.2018.07.004

Haine, T. W. N., & Marshall, J. (1998). Gravitational, symmetric, and baroclinic instability of the ocean mixed layer. *Journal of Physical Oceanography*, *28*(4), 634–658. https://doi.org/10.1175/1520-0485(1998)028<0634:Gsabio>2.0.Co;2

Hong, H. S., Chai, F., Zhang, C. Y., Huang, B. Q., Jiang, Y. W., & Hu, J. Y. (2011). An overview of physical and biogeochemical processes and ecosystem dynamics in the Taiwan Strait. *Continental Shelf Research*, *31*(6), S3–S12. https://doi.org/10.1016/j.csr.2011.02.002

Hong, H. S., Liu, X., Chiang, K. P., Huang, B. Q., Zhang, C. Y., Hu, J., & Li, Y. H. (2011b). The coupling of temporal and spatial variations of chlorophyll a concentration and the East Asian monsoons in the southern Taiwan Strait. *Continental Shelf Research*, *31*(6), S37–S47. https://doi.org/10.1016/j.csr.2011.02.004

Hoskins, B. J. (1974). The role of potential vorticity in symmetric stability and instability. *Quarterly Journal of the Royal Meteorological Society*, *100*(425), 480–482. https://doi.org/10.1002/qj.49710042520

Hu, J. Y. (2002). *Study of marine dynamical environmental characteristics in the Taiwan Strait and adjacent waters*. Ph. D Dissertation, Xiamen University. (in Chinese with English abstract).

Hu, J. Y., Kawamura, H., Li, C. Y., Hong, H. S., & Jiang, Y. W. (2010). Review on current and seawater volume transport through the Taiwan Strait. *Journal of Oceanography*, *66*(5), 591–610. https://doi.org/10.1007/s10872-010-0049-1

Huang, B. Y., Liu, C. Y., Banzon, V., Freeman, E., Graham, G., Hankins, B., et al. (2021). Improvements of the daily Optimum Interpolation sea surface temperature (DOISST) version 2.1. *Journal of Climate*, *34*(8), 2923–2939. https://doi.org/10.1175/jcli-d-20-0166.1

Huang, S. M., & Oey, L. Y. (2015). Right-side cooling and phytoplankton bloom in the wake of a tropical cyclone. *Journal of Geophysical Research-Oceans*, *120*(8), 5735–5748. https://doi.org/10.1002/2015jc010896

Huisman, J., Sharples, J., Stroom, J. M., Visser, P. M., Kardinaal, W. E. A., Verspagen, J. M. H., & Sommeijer, B. (2004). Changes in turbulent mixing shift competition for light between phytoplankton species. *Ecology*, *85*(11), 2960–2970. https://doi.org/10.1890/03-0763

Huisman, J., van Oostveen, P., & Weissing, F. J. (1999). Critical depth and critical turbulence: Two different mechanisms for the development of phytoplankton blooms. *Limnology & Oceanography*, *44*(7), 1781–1787. https://doi.org/10.4319/lo.1999.44.7.1781

Hydes, D. J., & Hill, N. C. (1985). Determination of nitrate in seawater - nitrate to nitrite reduction with copper-cadmium alloy. *Estuarine, Coastal and Shelf Science*, *21*(1), 127–130. https://doi.org/10.1016/0272-7714(85)90011-3

Ji, W. D., & Huang, S. G. (1992). The characteristics of nutrients variation in the Western Taiwan Strait IV. The influence of water mixing and phytoplankton consumption to the ratio of Si, N and P. *Acta Oceanologica Sinica*, *14*, 53–62. (in Chinese).

Kanamitsu, M., Ebisuzaki, W., Woollen, J., Yang, S. K., Hnilo, J. J., Fiorino, M., & Potter, G. L. (2002). NCEP-DOE AMIP-II reanalysis (R-2). *Bulletin America Meteorology Social*, *83*(11), 1631–1643. https://doi.org/10.1175/bams-83-11-1631

Kohonen, T. (1998). The self-organizing map. *Neurocomputing*, *21*(1–3), 1–6. https://doi.org/10.1016/s0925-2312(98)00030-7

Kohonen, T. (2013). Essentials of the self-organizing map. *Neural Networks*, *37*, 52–65. https://doi.org/10.1016/j.neunet.2012.09.018

Koseki, S., Giordani, H., & Goubanova, K. (2019). Frontogenesis of the Angola-Benguela frontal zone. *Ocean Science*, *15*(1), 83–96. https://doi.org/10.5194/os-15-83-2019

Kuang, F. F., Zhang, Y. Q., Zhang, J. P., & Jia, C. (2015). Comparison and evaluation of three sea surface wind products in Taiwan Strait. *Hai Yang Xue Bao*, *37*(5), 44–53. (in Chinese). https://doi.org/10.3969/j.issn.0253-4193.2015.05.005

Levy, M., Ferrari, R., Franks, P. J. S., Martin, A. P., & Riviere, P. (2012). Bringing physics to life at the submesoscale. *Geophysical Research Letters*, *39*(14), 13. https://doi.org/10.1029/2012gl052756

Lewis, M. R., Horne, E. P. W., Cullen, J. J., Oakey, N. S., & Platt, T. (1984). Turbulent motions may control phytoplankton photosynthesis in the upper ocean. *Nature*, *311*(5981), 49–50. https://doi.org/10.1038/311049a0

Liao, E. H., Jiang, Y. W., Li, L., Hong, H. S., & Yan, X. H. (2013). The cause of the 2008 cold disaster in the Taiwan Strait. *Ocean Modelling*, *62*, 1–10. https://doi.org/10.1016/j.ocemod.2012.11.004

Lin, X. Y., Yan, X. H., Jiang, Y. W., & Zhang, Z. C. (2016). Performance assessment for an operational ocean model of the Taiwan Strait. *Ocean Modelling*, *102*, 27–44. https://doi.org/10.1016/j.ocemod.2016.04.006

Liu, K. K., Chao, S. Y., Shaw, P. T., Gong, G. C., Chen, C. C., & Tang, T. Y. (2002). Monsoon-forced chlorophyll distribution and primary production in the South China Sea: Observations and a numerical study. *Deep-Sea Research Part I*, *49*(8), 1387–1412. https://doi.org/10.1016/s0967-0637(02)00035-3

Liu, Y., & Weisberg, R. (2011). A review of self-organizing map applications in meteorology and oceanography, edited, https://doi.org/10.5772/13146

Liu, Y., Weisberg, R., & Mooers, C. (2006). Performance evaluation of the self-organizing map for feature extraction. *Journal of Geophysical Research*, *111*(C5), C05018. https://doi.org/10.1029/2005JC003117

Longhurst, A., Sathyendranath, S., Platt, T., & Caverhill, C. (1995). AN estimate of global primary production in the ocean from satellite radiometer data. *Journal of Plankton Research*, *17*(6), 1245–1271. https://doi.org/10.1093/plankt/17.6.1245

Lu, W. F., Luo, Y. W., Yan, X. H., & Jiang, Y. W. (2018). Modeling the contribution of the microbial carbon pump to carbon sequestration in the South China Sea. *Science China Earth Sciences*, *61*(11), 1594–1604. https://doi.org/10.1007/s11430-017-9180-y

Lu, W. F., Oey, L. Y., Liao, E. H., Zhuang, W., Yan, X. H., & Jiang, Y. W. (2018). Physical modulation to the biological productivity in the summer Vietnam upwelling system. *Ocean Science*, *14*(5), 1303–1320. https://doi.org/10.5194/os-14-1303-2018

Lu, W. F., Su, H., Yang, X., & Yan, X. H. (2019). Subsurface temperature estimation from remote sensing data using a clustering-neural network method. *Remote Sensing of Environment*, *229*, 213–222. https://doi.org/10.1016/j.rse.2019.04.009

Lu, W. F., Yan, X. H., Han, L., & Jiang, Y. W. (2017). One-dimensional ocean model with three types of vertical velocities: A case study in the South China Sea. *Ocean Dynamics*, *67*(2), 253–262. https://doi.org/10.1007/s10236-016-1029-9

Lu, W. F., Yan, X. H., & Jiang, Y. W. (2015). Winter bloom and associated upwelling northwest of the Luzon island: A coupled physical-biological modeling approach. *Journal of Geophysical Research-Oceans*, *120*(1), 533–546. https://doi.org/10.1002/2014jc010218

Mahadevan, A. (2006). Modeling vertical motion at ocean fronts: Are nonhydrostatic effects relevant at submesoscales? *Ocean Modelling*, *14*(3–4), 222–240. https://doi.org/10.1016/j.ocemod.2006.05.005

Mahadevan, A. (2016). The impact of submesoscale physics on primary productivity of plankton. In C. A. Carlson & S. J. Giovannoni (Eds.), *Annual Review of Marine Science* (Vol. 8, pp. 161–184). Annual Reviews. https://doi.org/10.1146/annurev-marine-010814-015912

Mahadevan, A., D'Asaro, E., Lee, C., & Perry, M. J. (2012). Eddy-driven stratification initiates north Atlantic spring phytoplankton blooms. *Science*, *337*(6090), 54–58. https://doi.org/10.1126/science.1218740

Mahadevan, A., Tandon, A., & Ferrari, R. (2010). Rapid changes in mixed layer stratification driven by submesoscale instabilities and winds. *Journal of Geophysical Research-Oceans*, *115*(C3), 12. https://doi.org/10.1029/2008jc005203

McWilliams, J. C. (2016). Submesoscale currents in the ocean. *Proceedings of the Royal Society A-Mathematical Physical and Engineering Sciences*, *472*(2189), 32. https://doi.org/10.1098/rspa.2016.0117

Mellor, G. L., & Yamada, T. (1982). Development of a turbulence closure-model for geophysical fluid problems. *Reviews Geophysics*, *20*(4), 851–875. https://doi.org/10.1029/RG020i004p00851

Molemaker, M. J., McWilliams, J. C., & Yavneh, I. (2005). Baroclinic instability and loss of balance. *Journal of Physical Oceanography*, *35*(9), 1505–1517. https://doi.org/10.1175/jpo2770.1

Morel, A., & Berthon, J. F. (1989). Surface pigments, algal biomass profiles, and potential production of the euphotic layer—relationships reinvestigated in view of remote-sensing applications. *Limnology & Oceanography*, *34*(8), 1545–1562. https://doi.org/10.4319/lo.1989.34.8.1545

Oey, L. Y. (2008). Loop current and deep eddies. *Journal of Physical Oceanography*, *38*(7), 1426–1449. https://doi.org/10.1175/2007jpo3818.1

Oey, L. Y., Chang, M. C., Chang, Y. L., Lin, Y. C., & Xu, F. H. (2013). Decadal warming of coastal China Seas and coupling with winter monsoon and currents. *Geophysical Research Letters*, *40*(23), 6288–6292. https://doi.org/10.1002/2013gl058202

Oey, L. Y., Chang, Y. L., Lin, Y. C., Chang, M. C., Varlamov, S., & Miyazawa, Y. (2014). Cross flows in the Taiwan Strait in winter. *Journal of Physical Oceanography*, *44*(3), 801–817. https://doi.org/10.1175/jpo-d-13-0128.1

Orlanski, I., & Cox, M. D. (1972). Baroclinic instability in ocean currents. *Geophysical Fluid Dynamics*, *4*, 297–332. https://doi.org/10.1080/03091927208236102

Reusch, D., Alley, R., & Hewitson, B. (2005). Relative performance of self-organizing maps and principal component analysis in pattern extraction from synthetic climatological data. *Polar Geography*, *29*(3), 188–212. https://doi.org/10.1080/789610199

Sabine, C. L., Feely, R. A., Gruber, N., Key, R. M., Lee, K., Bullister, J. L., et al. (2004). The oceanic sink for anthropogenic CO_2. *Science*, *305*(5682), 367–371. https://doi.org/10.1126/science.1097403

Shchepetkin, A. F., & McWilliams, J. C. (2003). A method for computing horizontal pressure-gradient force in an oceanic model with a nonaligned vertical coordinate. *Journal of Geophysical Research-Oceans*, *108*(C3), 34. https://doi.org/10.1029/2001jc001047

Shchepetkin, A. F., & McWilliams, J. C. (2005). The regional oceanic modeling system (ROMS): A split-explicit, free-surface, topography-following-coordinate oceanic model. *Ocean Modelling*, 9(4), 347–404. https://doi.org/10.1016/j.ocemod.2004.08.002

Smagorinsky, J. (1963). General circulation experiments with the primitive equations: I. The basic experiment. *Monthly Weather Review*, *91*(3), 99–164. https://doi.org/10.1175/1520-0493(1963)091<0099:GCEWTP>2.3.CO;2

Smith, S. V. (1984). Phosphorus versus nitrogen limitation in the marine-environment. *Limnology & Oceanography*, *29*(6), 1149–1160. https://doi.org/10.4319/lo.1984.29.6.1149

Solidoro, C., Bandelj, V., Barbieri, P., Cossarini, G., & Umani, S. F. (2007). Understanding dynamic of biogeochemical properties in the northern Adriatic Sea by using self-organizing maps and k-means clustering. *Journal of Geophysical Research-Oceans*, *112*(C7), 13. https://doi.org/10.1029/2006jc003553

Song, Y., & Haidvogel, D. (1994). A semi-implicit ocean circulation model using a generalized topography-following coordinate system. *Journal of Computational Physics*, *115*(1), 228–244. https://doi.org/10.1006/jcph.1994.1189

Stewart, R. (2008). Introduction to Physical Oceanography (p. 353). https://doi.org/10.1119/1.18716

Stone, P. H. (1966). On non-geostrophic baroclinic stability. *Journal of Atmosphere*, *23*(4), 390–400. https://doi.org/10.1175/1520-0469(1966)023<0390:ongbs>2.0.co;2

Stone, P. H. (1970). On non-geostrophic baroclinic stability: Part II. *Journal of the Atmospheric Sciences*, *27*(5), 721–726. https://doi.org/10.1175/1520-0469(1970)027<0721:ongbsp>2.0.co;2

Strom, S. L., Brainard, M. A., Holmes, J. L., & Olson, M. B. (2001). Phytoplankton blooms are strongly impacted by microzooplankton grazing in coastal North Pacific waters. *Marine Biology*, *138*(2), 355–368. https://doi.org/10.1007/s002270000461

Sun, J., Liu, D. Y., Wang, Z. L., Shi, X. Y., Li, R. X., & Zhu, M. Y. (2003). Microzooplankton herbivory during red tide-frequent-occurrence period in Spring in the East China Sea. *Chinese Journal of Applied Ecology*, *14*(7), 1073–1080. (in Chinese). https://doi.org/10.3969/j.issn.0253-4193.2015.05.005

Sverdrup, H. (1953). On conditions for the vernal blooming of phytoplankton. *ICES Journal of Marine Science*, *18*(3), 287–295. https://doi.org/10.1093/icesjms/18.3.287

Tang, Y. X., Sun, H. L., Hu, X. M., Jiao, Y. T., Xiong, X. J., Liang, C. J., & Wang, W. Y. (2007). *Specifications for oceanographic survey. Part 2: Marine hydrographic observation, GB/T 12763.2–2007*. National Standardization of the P. R. China.

Tarry, D. R., Essink, S., Pascual, A., Ruiz, S., Poulain, P., Ozgokmen, T., et al. (2021). Frontal convergence and vertical velocity measured by drifters in the Alboran Sea. *Joural of Geophysical Research-Oceans*, *126*(4), 19. https://doi.org/10.1029/2020jc016614

Taylor, J. R., & Ferrari, R. (2009). On the equilibration of a symmetrically unstable front via a secondary shear instability. *Journal of Fluid Mechanics*, *622*, 103–113. https://doi.org/10.1017/s0022112008005272

Taylor, J. R., & Ferrari, R. (2010). Buoyancy and wind-driven convection at mixed layer density fronts. *Journal of Physical Oceanography*, *40*(6), 1222–1242. https://doi.org/10.1175/2010jpo4365.1

Taylor, J. R., & Ferrari, R. (2011a). Ocean fronts trigger high latitude phytoplankton blooms. *Geophysical Research Letters*, *38*(23), 5. https://doi.org/10.1029/2011gl049312

Taylor, J. R., & Ferrari, R. (2011b). Shutdown of turbulent convection as a new criterion for the onset of spring phytoplankton blooms. *Limnology & Oceanography*, *56*(6), 2293–2307. https://doi.org/10.4319/lo.2011.56.6.2293

Thomas, L. N., & Lee, C. M. (2005). Intensification of ocean fronts by down-front winds. *Journal of Physical Oceanography*, *35*(6), 1086–1102. https://doi.org/10.1175/jpo2737.1

Thomas, L. N., Taylor, J. R., Ferrari, R., & Joyce, T. M. (2013). Symmetric instability in the Gulf Stream. *Deep-Sea Research Part II*, *91*, 96–110. https://doi.org/10.1016/j.dsr2.2013.02.025

Wang, J., Hong, H. S., & Jiang, Y. W. (2016). A coupled physical-biological modeling study of the offshore phytoplankton bloom in the Taiwan Strait in winter. *Journal of Sea Research*, *107*, 12–24. https://doi.org/10.1016/j.seares.2015.11.004

Wang, J., Hong, H. S., Jiang, Y. W., Chai, F., & Yan, X. H. (2013). Summer nitrogenous nutrient transport and its fate in the Taiwan Strait: A coupled physical-biological modeling approach. *Journal of Geophysical Research-Oceans*, *118*(9), 4184–4200. https://doi.org/10.1002/jgrc.20300

Wang, T., Yu, P., Wu, Z., Lu, W., Liu, X., Li, Q., & Huang, B. (2021). Revisiting the intraseasonal variability of chlorophyll-a in the adjacent Luzon strait with a new gap-filled remote sensing data set. *IEEE Transactions on Geoscience and Remote Sensing*, *60*, 1–11. https://doi.org/10.1109/TGRS.2021.3067646

Welschmeyer, N. A. (1994). Fluorometric analysis of chlorophyll-a in the presence of chlorophyll-B and pheopigments. *Limnology & Oceanography*, *39*(8), 1985–1992. https://doi.org/10.4319/lo.1994.39.8.1985

Wu, H., Deng, B., Yuan, R., Hu, J., Gu, J. H., Shen, F., et al. (2013). Detiding measurement on transport of the Changjiang-derived buoyant coastal current. *Journal of Physical Oceanography*, *43*(11), 2388–2399. https://doi.org/10.1175/jpo-d-12-0158.1

Yang, J. Y. (2007). An oceanic current against the wind: How does Taiwan island steer warm water into the East China Sea? *Journal of Physical Oceanography*, *37*(10), 2563–2569. https://doi.org/10.1175/jpo3134.1

Yin, Y. Q., Lin, X. P., Li, Y. Z., & Zeng, X. M. (2014). Seasonal variability of Kuroshio intrusion northeast of Taiwan Island as revealed by self-organizing map. *Chinese Journal of Oceanology and Limnology*, *32*(6), 1435–1442. https://doi.org/10.1007/s00343-015-4017-x

Zeng, X., Li, Y., He, R., & Yin, Y. (2015). Clustering of Loop Current patterns based on the satellite-observed sea surface height and self-organizing map. *Remote Sensing Letters*, *6*(1), 11–19. https://doi.org/10.1080/2150704x.2014.998347

Zeng, X. B., & Huang, B. Q. (2012). Grazing impact of microzooplankton on different pigment groups of phytoplankton in the south Taiwan Strait in summer. *Marine Sciences*, *36*(8), 28–34. (in Chinese). https://doi.org/10.3969/j.issn.0253-4193.2015.05.005

Zeng, X. B., Huang, B. Q., Chen, J. X., & Hong, H. S. (2006). Grazing impact of microzooplankton on algal bloom in the Taiwan Strait in summer. *Acta Oceanologica Sinica*, *28*(5), 107–116. (in Chinese). https://doi.org/10.3969/j.issn.0253-4193.2015.05.005

Zhang, C. Y., Hu, C. M., Shang, S. L., Muller-Karger, F. E., Li, Y., Dai, M. H., et al. (2006). Bridging between SeaWiFS and MODIS for continuity of chlorophyll-a concentration assessments off Southeastern China. *Remote Sensing of Environment*, *102*(3–4), 250–263. https://doi.org/10.1016/j.rse.2006.02.015

Zhang, F. (2001). Seasonal variation features of chlorophyll a content in Taiwan Strait. *Journal of Oceanography in Taiwan Strait*, *20*, 314–318. (in Chinese with English abstract).

Zhang, F., & Huang, B. Q. (2000). Affect of Hydrologic characteristics for the distribution and variability of chlorophyll a in the northern part of Taiwan Strait in winter. *Marine Sciences*, *24*, 1–3. (in Chinese).

Zhao, Z. H., Lin, J. W., Fu, J., & Jiang, Y. W. (2020). Cold water anomalies in the middle layer of the northern Taiwan Strait in spring-a numerical approach. *Ocean Dynamics*, *70*(12), 1571–1585. https://doi.org/10.1007/s10236-020-01412-1

Zheng, L. P., Xiang, W. G., & Huang, B. Q. (2012). Grazing pressure of microzooplankton on phytoplankton in northern South China Sea in winter. *Journal of Oceanography in Taiwan Strait*, *31*(1), 72–78. (in Chinese). https://doi.org/10.3969/j.issn.0253-4193.2015.05.005